The Dissertation Committee for Qi Ren Certifies that this is the approved version of the following dissertation:

Anisotropic seismic characterization of the Eagle Ford Shale: rock-physics modeling, stochastic seismic inversion, and geostatistics

Committee:

Mrinal K. Sen, Supervisor

Kyle T. Spikes, Co-Supervisor

Sanjay Srinivasan

Sergey Fomel

Hugh Daigle

Anisotropic seismic characterization of the Eagle Ford Shale: rock-physics modeling, stochastic seismic inversion, and geostatistics

by

Qi Ren, B.S.

Dissertation

Presented to the Faculty of the Graduate School of

The University of Texas at Austin

in Partial Fulfillment

of the Requirements

for the Degree of

Doctor of Philosophy

The University of Texas at Austin

May 2016

Dedication

To my family

Acknowledgements

This is my 6th year at The University of Texas at Austin. I was a PhD student in major of physics for the first one and half years; then I transferred to geophysics in January 2012. There are many people who have helped me during this time. I would like to express my sincere appreciation to them.

First and foremost, I would like to thank my advisors Dr. Mrinal Sen and Dr. Kyle Spikes. With their outstanding guidance, suggestions, and encouragement, I have had great opportunities to explore geophysics and unconventional reservoirs. I first contacted Dr. Sen for a possible research opportunity. In the following two months, we met with each other every week to discuss good papers and basic knowledge in seismic exploration. Dr. Sen introduced me to the world of geophysics, and then he introduced me to Dr. Kyle Spikes before he went to India. I worked with Kyle for the rock physics modeling part of my dissertation. Kyle has been a mentor, colleague, and a friend. He is always so kind, patient, and encouraging. Besides rock physics, I learned how to prepare presentations and write technical papers from Kyle. He is very patient when helping me to modify presentation slides and edit papers. I can clearly feel my improvement on these two areas during the 4 years in Jackson School of Geosciences. After Dr. Sen came back to UT, I worked with him on the seismic inversion part of my dissertation. Dr. Sen is very knowledgeable and intelligent in seismic inversion. He always hits the point, and his suggestions are always helpful. He is always patient and kind for my questions. In addition, he showed me how hard work can be rewarding.

I would like to thank my dissertation committee members, Dr. Sanjay Srinivasan, Dr. Sergey Fomel, and Dr. Hugh Daigle for their support and help on my PhD research. In particular, Dr. Sanjay Srinivasan collaborated with us on the SUTUR project for the geostatistical part of the research. The committee's feedback and comments were very helpful in improving this dissertation.

During my graduate studies, I took many useful classes from excellent teachers. I want to express my deep appreciation to them: Dr. Robert Tatham, Dr. Paul Stoffa, Dr. Stephen Grand, Dr. William Fisher, and Dr. Charles Kerans in the Jackson School of Geosciences (JSG), Dr. Sanjay Srinivasan, and Dr. Hugh Daigle in the Department of Petroleum and Geosystems Engineering, and the parallel computer group in the Texas Advanced Computing Center (TACC). The knowledge I learned from their classes has turned out to be very useful to my research.

I would like to thank Thomas Hess to help me manage the database, and to teach me how to use software packages in the geophysical laboratory, such as Landmark, and Hampson Russell. I would like to thank our graduate coordinator Philip Guerrero. He helped me a lot on various class forms, class registration, financial support applications, and graduation procedures.

I would like to give special thanks to Yi Tao and Shaoping Lu to encourage me and help me during the transition time from the physics department to the Jackson School of Geosciences.

I would like to thank Morteza Naraghi for collaboratign with me on the geostastical part of my dissertation, and Shuang Gao in Dr. Carlos Torres-Verdin's group to provide us with the petrophysical inverted rock composition.

I enjoyed discussing research and having fun with the following students and postdoc fellows in Jackson School of Geosciences. My thanks goes to, but not limited to, Meijuan Jiang, Russell Cater, Kwon Taek Oh, Sarah Coyle, Lauren Becker, Jacqueline Maleski, Patrick Gustie, Makoto Sadahiro, Yang Xue, YI Tao, Sharif Morshed, Kumar Das, Mohammed Alhussain, Rui Zhang, Youcai Tang, Yu Xia, Xiaolei Song, Yang Wang, Siwei Li, Jiao Xue, Karl Oskar Sletten, Badr Alulaiw, Anthony Barone, Bei Pan, Reetam Biswas, Barry Borgman, Elliot Dahl, Debanjan Datta, Han Liu, David Tang, Andrew Yanke, Zeyu Zhao, Chang Lu, Dmitrii Merzlikin, Yanadet Sripanich, Junzhe Sun, Zhiguang Xue, Kelly Regimbal, Yangkang Chen, Luke Decker, Ruohan Gao, Ryan Swindeman, Tieyuan Zhu, Yawen He, Hejun Zhu. Thank you all for making my life bright.

Thanks to Shell for providing the research data, financial support, and permission for publication. Special thanks goes to Ronny Hofmann for coordinating with us on the Shell side of the SUTUR project.

Last but not least, I would like to thank my husband, Chao Fang, my parents, Junmei Wang and Songbai Ren, for their love and support.

Anisotropic seismic characterization of the Eagle Ford Shale: rock-physics modeling, stochastic seismic inversion, and geostatistics

Qi Ren, Ph.D

The University of Texas at Austin, 2016

Supervisors: Mrinal K. Sen, Kyle T. Spikes

Quantitative reservoir characterization using integrated seismic data and well log data is important in sweet spot identification, well planning, and reservoir development. The process includes building up the relations between rock properties and elastic properties through rock physics modeling, inverting for elastic properties from seismic data, and inverting for rock properties from both seismic data and rock physics models. Many quantitative reservoir characterization techniques have been developed for conventional reservoirs. However, challenges remain when extending these methods to unconventional reservoirs because of their complexity, such as anisotropy, micro-scale fabric, and thin beds issues. This dissertation focuses on developing anisotropic rock physics modeling method and seismic inversion method that are appliable for unconventional reservoir characterization.

The micro-scale fabric, including the complex composition, shape and alignment of clay minerals, pore space, and kerogen, significantly influences the anisotropic elastic properties. I developed a comprehensive three-step rock-physics approach to model the anisotropic elastic properties, accounting for the micro-scale fabric. In addition, my method accounts for the different pressure-dependent behaviors of P-waves and S-waves.

The modeling provides anisotropic stiffnesses and pseudo logs of anisotropy parameters. The application of this method on the Upper Eagle Ford Shale shows that the clay content kerogen content and porosity decrease the rock stiffness. The anisotropy increases with kerogen content, but the influence of clay content is more complex. Comparing the anisotropy parameter pseudo logs with clay content shows that clay content increases the anisotropy at small concentrations; however, the anisotropy stays constant, or even slightly decreases, as clay content continues to increase.

Thin beds and anisotropy are two important limitation of the application of seismic characterization on unconventional reservoirs. I introduced the geostatistics into stochastic seismic inversion. The geostatistical models, based on well log data, simulate small-scale vertical variations that are beyond seismic resolution. This additional information compensates the seismic data for its band-limited nature. I applied this method on the Eagle Ford Shale, using greedy annealing importance sampling as inversion algorithm. The thin Lower Eagle Ford Formation, which cannot be resolved by conventional inversion method, is clearly resolved in the inverted impedance volume using my method. In addition, because anisotropy is accounted for in the forward modeling, the accuracy of inverted S-impedance is significantly improved.

Table of Contents

List of Tables

List of Figures

Chapter 1: Introduction

1.1 OBJECTIVE AND MOTIVATION

Quantitative reservoir characterization using integrated seismic data and well log data is important in sweet spot identification, well planning, and reservoir development. The purpose of quantitative reservoir characterization is to provide rock property maps of the reservoir and assess fluid content. The process includes building up the relations between rock properties, for example, porosity, clay content, kerogen content, and elastic properties through rock physics modeling, inverting for elastic properties from seismic data, and inverting for rock properties from both seismic data and rock physics models. Many quantitative reservoir characterization techniques have been developed for conventional reservoirs (Mukerji et al., 2001, Bachrach 2006, Spikes et al., 2007, Grana and Rossa, 2010). However, challenges remain when extending these methods to unconventional reservoirs because of their complexity, such as anisotropy, micro-scale fabric, and thin-bed issues.

Seismic velocity measurements in the laboratory indicate that shale exhibits vertical transversely isotropic (VTI) symmetry, with the symmetry axis perpendicular to bedding direction (e.g., Vernik and Nur, 1992, Hornby, 1998, Dewhurst and Siggins, 2006, Jones and Wang, 1981, and Wang, 2002). This elastic anisotropy controls seismic wave propagation and thus affects elastic wave amplitudes, travel times and ray paths (Banik, 1984, Sayers, 2005). Micro-structural studies have demonstrated complex morphologies and fabrics (e.g., Chalmers et al., 2012; Sondergeld et al., 2010). In the two cases in Chalmers et al. (2012) and Sondergeld et al. (2010), and in others, the complex fabric is likely the cause of the elastic anisotropy. The other issue for unconventional reservoir characterization is thin beds. Seismic data are one of the key datasets for

quantitative reservoir characterization. Because of its band-limited nature, seismic data cannot resolve thin layers below one-eighth of a wavelength in thickness (Widess, 1973). However, such thin layers might be significant reservoirs or sweet spots in unconventional reservoirs. The Eagle Ford Shale in the study area of this project is an example of this thin-bed issue. The Eagle Ford Shale is an upper Cretaceous shale located in south Texas. It is overlain by the Austin Chalk and underlain by the Buda Limestone (Hentz and Ruppel, 2010). The Eagle Ford contains two sub-formations: the Upper Eagle Ford and Lower Eagle Ford. Although both the Upper and Lower Eagle Ford are hydrocarbon reservoirs, the Lower Eagle Ford contains higher organic content and higher porosity. In the study area of this project, the Lower Eagle Ford is a thin layer with thickness varying from 0 to 40ft. The seismic data do not resolve this thin layer. Resolving this thin Lower Eagle Ford is critical for quantitative reservoir characterization.

Although many challenges exist, ideas and techniques used in conventional reservoir quantitative characterization can still be used for unconventional reservoir characterization. Mukerji et al. (2001) introduced statistical techniques combined with log data and seismic information for quantitative reservoir characterization. This quantitative reservoir characterization framework contained three steps. Firstly, they defined the lithofacies based on well logs. Secondly, they derived the acoustic and elastic impedances from seismic data. Finally, they simulated the lithofacies distributions on inverted impedance cubes using a statistical approach. The final results were probability maps of the lithofacies. They applied this method to a North Sea turbidite system. In this work, they used statistical Bayesian classification to define lithofacies based on impedance and Vp/Vs, and extended the training data from log measurements to the entire model space by Gassmann's equation. Impedance here refers to density times the

vertical propagation velocity of P- and S-wave; and Vp/Vs refers the ratio of vertical propagation velocity between P- and S-wave. The poststack inversion was done on a near-offset stack and far offset stack independently to obtain the acoustic impedance and elastic impedance volumes, using generalized least-squares inversion. Finally, geostatistical classification and simulation were applied to combine the training data and inverted impedance volumes in order to provide the spatial maps of most likely lithofacies and their occurrence probabilities. The geostatistical approach includes quadratic discriminant analysis, probability estimation based on the probability density functions for each facies, and a geostatistical indicator simulation to incorporate the spatial correlation of these faces. The three-step quantitative reservoir characterization framework became a standard process. Application of the framework could vary from reservoir to reservoir in terms of different rock physics models, inversion algorithms, and the statistical techniques. The choice of these detailed techniques should be based on careful analysis of the reservoir geological environment and data available.

Bachrach (2006) applied quantitative interpretation to a clastic system for joint estimation of porosity and saturation. He showed that the porosity and saturation depended on each other; therefore, they should be inverted simultaneously. He used a Monte Carlo method to explore the joint distribution of porosity and saturation at all possible value ranges. The simulation results showed that the porosity estimation, based on inverted P- and S- impedance and density from seismic data, had smaller uncertainty than the saturation estimation. Spikes et al. (2007) developed a probabilistic seismic inversion method, which integrated rock physics models based on a Bayesian formulation for a clastic environment. This approach differed from Mukerji et al. (2001) in that Spikes et al. (2007) involved the rock physics modeling as a part of the seismic inversion. The model parameters for seismic inversion were rock properties (clay content, porosity,

and water saturation), instead of P-, S- impedance and density. The rock physics model provided the link between impedances and rock properties, based on which, each prior model of rock properties corresponded to a specified set of impedances. Synthetic seismograms generated from rock properties were compared to measured seismograms to calculate the likelihood functions. The posterior distributions of the best-fitting rock property models were obtained through acceptance or rejection in a full-grid search. Spikes at al. (2007) tested this method on well and seismic data from offshore western South Africa. They assumed the formation thickness was constant through the reservoir, and the reservoir was isotropic and homogeneous.

Quantitative reservoir characterization for unconventional reservoirs is much more complex than for conventional reservoir. A few studies integrate anisotropic rock-physics modeling and anisotropic seismic analysis for unconventional reservoirs. Bachrach et al. (2013) built a workflow for quantitative interpretation of unconventional reservoirs with integrating seismic inversion and rock physics modeling through wide-azimuth, long offset-seismic data. In the workflow, a suitable inversion algorithm was first applied to the wide azimuth seismic data, and then the reservoir properties of interest were estimated by stochastic anisotropic rock physics modeling combined with the inversion results. The case study was from the Bakken Shale where they estimated high-resolution fracture density and total porosity. Jiang (2014) and Jiang and Spirke (2013) investigated the seismic scale rock properties for the Haynesville Shale by integrating rock physics modeling, grid searching, and seismic inversion. In the rock physics modeling, she used the self-consistent (O'Connell and Budiansky, 1974) model to account for the various shapes and sizes of grains and pores; then she applied Chapman's model (Chapman, 2003) to build up a medium by introducing aligned fractures.

However, the seismic inversion algorithm she used was isotropic. The Hayesville Shale is a thick formation in her study area; therefore, thin beds were not an issue in her study.

Directional velocity measurements from the laboratory in the study area of this dissertation showed that the Eagle Ford Shale exhibits VTI symmetry. Thomsen (1986) introduced three parameters (ε, γ, and δ) to describe the anisotropy. ε represents the P-wave anisotropy, γ represents S-wave anisotropy, and δ represents a combination of P-wave and S-wave anisotropy. In the study area, the measured ε is about 0.15 for the Upper Eagle Ford and 0.31 for the Lower Eagle Ford; measured δ is about 0.07 for the Upper Eagle Ford and 0.15 for the Lower Eagle Ford. The anisotropy is highly influenced by the shale micro-scale fabric, including complex composition, platy clay minerals, kerogen, and their preferred orientation patterns. The shale micro-scale fabric requires a comprehensive rock physics modeling method. In addition, thin beds are another challenge in Eagle Ford reservoir characterization. The Lower Eagle Ford, a target reservoir in the study area, is a thin layer with thickness varying from 0 to 40ft. This thin layer is not resolved from the seismic data. In this dissertation, I present a three-step comprehensive rock physics modeling method to account for the complex micro-scale fabric. For the thin bed issue, I present a geostatistics guided stochastic seismic inversion method to resolve the thin beds using inverted impedance.

The main contributions of this dissertation include: 1) development of a comprehensive rock physics modeling method that links the rock properties and anisotropic elastic properties in a complex micro-scale fabric framework; 2) introduction of geostatistics models, which contain small scale vertical variation, as a guide for seismic inversion. Thus the thin beds could be resolved in the inverted impedance domain.

1.2 CHAPTER DESCRIPTION

This dissertation broadly covers two main topics: anisotropic rock physics modeling (Chapter 3), and geostatistics guided stochastic seismic inversion (Chapter 4).

Chapter 2 introduces the study area and the data used in the project. The geologic background of the Eagle Ford Shale is reviewed. The data, including prestack and poststack seismic data from a 3D seismic survey, and well log data from three vertical wells, are described in detail. In addition, petrophysically inverted lithology and fluid saturation values at one of the three wells are presented in this chapter.

Chapter 3 investigates the anisotropic rock-physics relationships between elastic properties and rock properties in the Eagle Ford Shale accounting for the micro-scale fabric. The micro-scale fabric influences the elastic properties of rock formations. The complexity of the micro-scale fabric of shale results from composition, platy clay minerals, kerogen, and their preferred orientation patterns. This micro-scale fabric is also the likely cause of the elastic anisotropy of the rock. In Chapter 3, I present a comprehensive three-step rock-physics approach to model the anisotropic elastic properties of the Upper Eagle Ford Shale. The modeling provides anisotropic stiffnesses and pseudo logs of anisotropy parameters. Results show that the clay content, kerogen content and porosity decrease the rock stiffness. The anisotropy increases with kerogen content, but the influence of clay content is more complex. Comparing the anisotropy parameter pseudo logs with clay content shows that clay content increases the anisotropy at small concentrations; however, the anisotropy stays constant, or even slightly decreases, as clay content continues to increase. This result suggests that the preferred orientation of clay clusters is preserved at low clay concentration but vanishes at high clay concentration.

Chapter 4 presents a geostatistics guided seismic inversion method that aims to resolve thin beds and accounts for anisotropy. Thin-bed effects and anisotropy are two important factors limiting the use of conventional seismic characterization for the Eagle Ford Shale. To address these issues, I use the geostatistics guided greedy annealing importance sampling (GAIS) inversion. The geostatistical models simulate small-scale vertical variations that are beyond seismic resolution, which compensates for the band-limited nature of seismic data. The geostatical realizations of the well logs are used as a priori models, and the GAIS inversion quickly searches for the most probable pseudo-logs at all surface locations. GAIS first runs multiple independent very fast simulated annealing (VFSA), based on which grid importance sampling method was applied to explore the local best sample on the important regions. Finally, the weighted average of these local best samples provides the expected value of the target model distribution. This method provides an optimal balance between computational efficiency and accuracy of estimation. As for anisotropy, I used Ruger's (Ruger, 1997) VTI model to account for the anisotropy in the forward modeling. This geostatistics guided inversion was applied on pre-stack 3D seismic data to estimate the reservoir elastic properties and anisotropy parameters of the Eagle Ford Shale. In my results, the lower Eagle Ford is clearly resolved in the inverted impedance volume. The sharp boundary and large impedance contrast between the Eagle Ford and the Buda Limestone are also very clear in GAIS inverted impedances. In addition, because anisotropy was accounted for, in the forward modeling the quality of the inverted S-impedance significantly improved.

Chapter 5 presents the overall conclusions of the dissertation, as well as possible future work. The relationships between anisotropic rock properties and elastic properties of the Eagle Ford Shale are investigated.

Chapter 2: Study Area and Data

This chapter introduces the study area and the data used in my analysis, which is focused on the Eagle Ford Shale located in south Texas. The data used here include three vertical wells, post- and pre- stack 3D seismic data, and a velocity model. Two of the three wells (B4 and B7) are located in the seismic survey area, but the third well (B5) is out of the area. Data from well B5 contains both directly measured rock properties (like P- and S- wave velocities, and density) and petrophysically inverted lithology and fluid saturation. The other two wells contain only directly measured rock properties.

2.1 GEOLOGY

The Upper Cretaceous Eagle Ford Shale is located in the Maverick Basin and the adjacent San Marcos Arch in south Texas. It extends farther northeastward to the East Texas Basin (Figure 2.1) (Hentz and Ruppel, 2010). Sequence stratigraphic analysis separates the Eagle Ford Shale play area into two different regions (Figure 2.2). In the Maverick Basin and San Marcos Arch, the Austin Chalk overlays the Eagle Ford Shale, and the Buda Limestone underlies it. In the East Texas Basin, the Eagle Ford Shale is separated into the Eagle Ford Group, the Woodbine Group/Pepper Shale, and the Maness Shale. In both areas, the Eagle Ford Shale contains two sub-formations: the Upper Eagle Ford and the Lower Eagle Ford. The thickness of each sub-formation varies from location to location. The Upper Eagle Ford only exists in the area southwest of San Marcos Arch. Its unit thickness reaches a maximum in the Maverick Basin, and it thins towards the southeast. The Lower Eagle Ford is present thoughout most of the play area; its thickest peak is in the Maverick basin and it thins towards south and east. In the seismic survey area of this project, the Lower Eagle Ford is a thin layer that varies from 0 to 40 ft, but

the Upper Eagle Ford is much thicker. At well B5, the Upper and Lower Eagle Ford are about the same thickness (~ 80ft). Data for this work comes from the Maverick Basin.

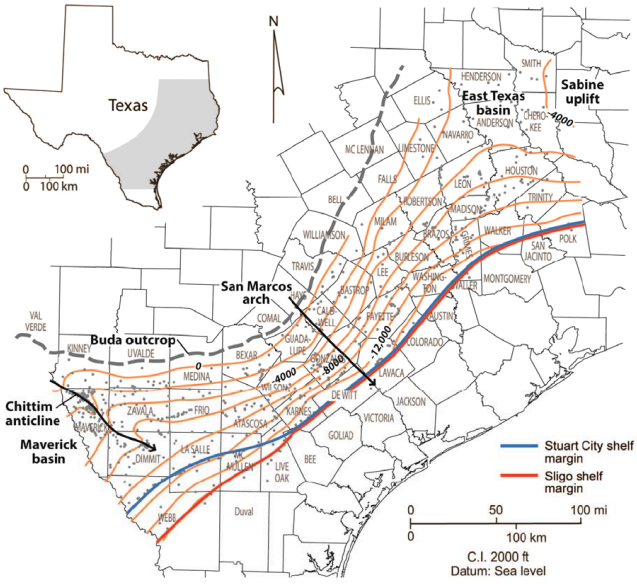

Figure 2.1: Location of the Eagle Ford Shale (Hentz and Ruppel, 2010). The Eagle Ford Shale is located in the Maverick Basin and San Marcos Arch in south Texas and extends to the east Texas Basin to the northeast. Our study area is located in the Maverick Basin, which is in the southwest of this map. The orange lines show the contours of the base of the Eagle Ford Shale.

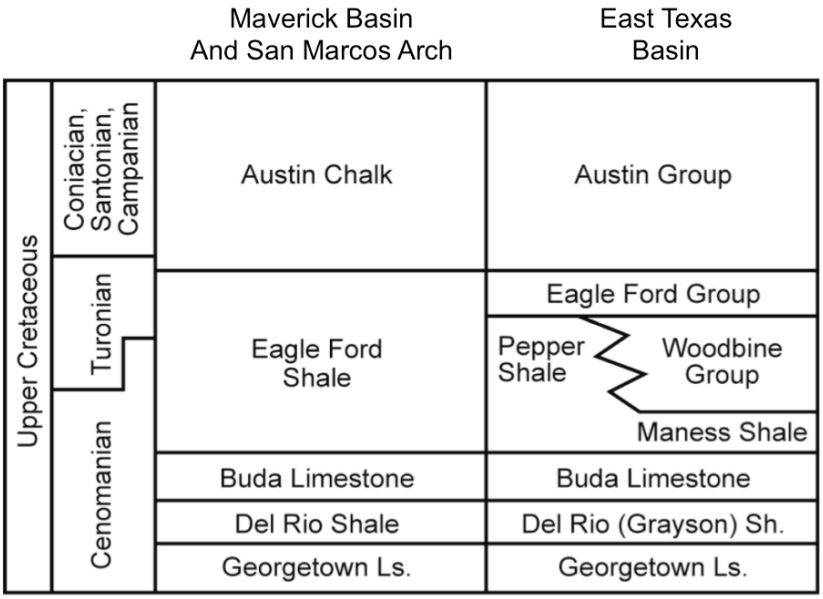

Figure 2.2: Conventional lithostratigraphy of the Eagle Ford Shale (Hentz and Ruppel, 2010). Stratigraphically, the Austin Chalk overlays the Eagle Ford Shale, and the Buda Limestone underlies it. Different from in the Maverick Basin and the San Marcos arch, in the East Texas Basin, the Eagle Ford Shale is separated into the Eagle Ford Group, the Woodbine Group/Pepper Shale, and the Maness Shale. Generally, the Lower Eagle Ford has higher organic content and porosity than the Upper Eagle Ford. Also, their coverage areas are different.

The Lower Eagle Ford consists mostly of dark-gray organic rich mudrock, with generally high gamma-ray values. The Upper Eagle Ford interval is characterized by overall lower gamma-ray values relative to the lower, and consists of interbedded dark- and light-gray calcareous mudrock. Figure 2.3 shows a typical gamma ray log, resistivity log, and lithology of the Eagle Ford Shale in south Texas. Total organic content (TOC) values from outcrops of the lower Eagle Ford Shale at several localities near Austin in Travis County along the San Marcos Arch range from 1 to 8.3 wt%, with an average value of 2.8 wt%. Based on the gamma-ray, core data, and outcrop samples, the Lower Eagle Ford is found to be richer in organic content than the Upper Eagle Ford.

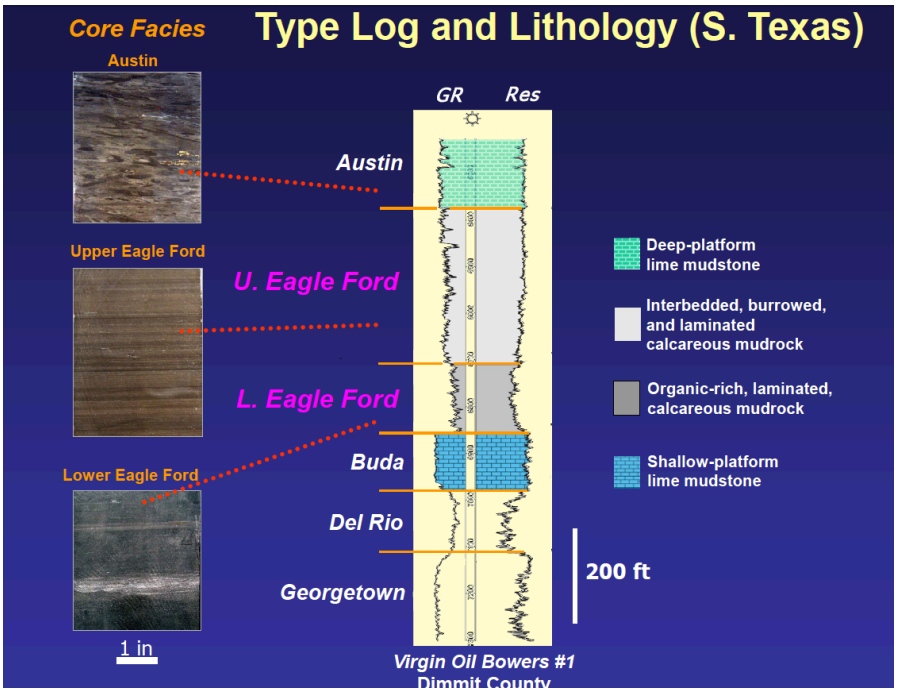

Figure 2.3: A typical log and lithology in the Eagle Ford in south Texas (Hentz and Ruppel, 2010). The Lower Eagle Ford consists mostly of dark-gray organic rich mudrock, with generally high gamma-ray values. The Upper Eagle Ford interval is characterized by overall lower gamma-ray values, relative to the lower, and consists of interbedded dark- and light-gray calcareous mudrock.

2.2 DATA DESCRIPTION

The data used in this project include pre-stack and post-stack 3D seismic data, a velocity model, and three vertical wells. Two of the three wells (B4 and B7) are located in the seismic survey area, but the third well (B5) is not. The full seismic data contains 1297 x 1001 traces. Each trace contains 2001 samples with a sample interval of 2ms, and the space between traces is 82.5ft. I picked the horizons (Austin Chalk, Eagle Ford, and Buda) based on post-stack seismic data; however, we do inversion only on a subsection of the seismic data, which contains 370 x 381 traces. This is based on two arguments: 1) computational cost; 2) the seismic data on the east end and west end are noisy, and it is difficult to pick the horizons. This subsection we chose covers both B4 and B7 wells, and it is large enough to demonstrate the objective for seismic inversion. The details of these data sets will be shown in this section.

2.2.1 Seismic data

Figure 2.4 is the map view of seismic data coverage used in the inversion analysis (the seismic survey coverage is much larger than this displayed area). The color in Figure 2.4 represents the depth of the Buda horizon in two way travel time. The top of the Buda dips towards the east. The other two horizons (Austin Chalk and Eagle Ford) have the same east-west dip. The relative locations of Wells B4 and B7 to the seismic survey are also shown in Figure 2.4. Well B4 is located in the northeast corner of the inversion window, and Well B7 is located in the southwest corner of the inversion window. Well B7 is relatively shallower than Well B4. The thickness variation of the Eagle Ford Shale in the inversion window, including both the Upper and Lower Eagle Ford, is shown in Figure 2.5. The thickness is measured in two way travel time (TWT). Although it is not

in the depth domain, the relative thickness variation in this area is clear. In the inversion window, the Eagle Ford Shale thickness is about 60m. Extended to the entire seismic survey area, the maximum thickness of Eagle Ford Shale is about 60ms (~ 120m) and minimum about 5ms (~ 10m). The lower Eagle Ford is too thin to pick on post-stack seismic amplitude data.

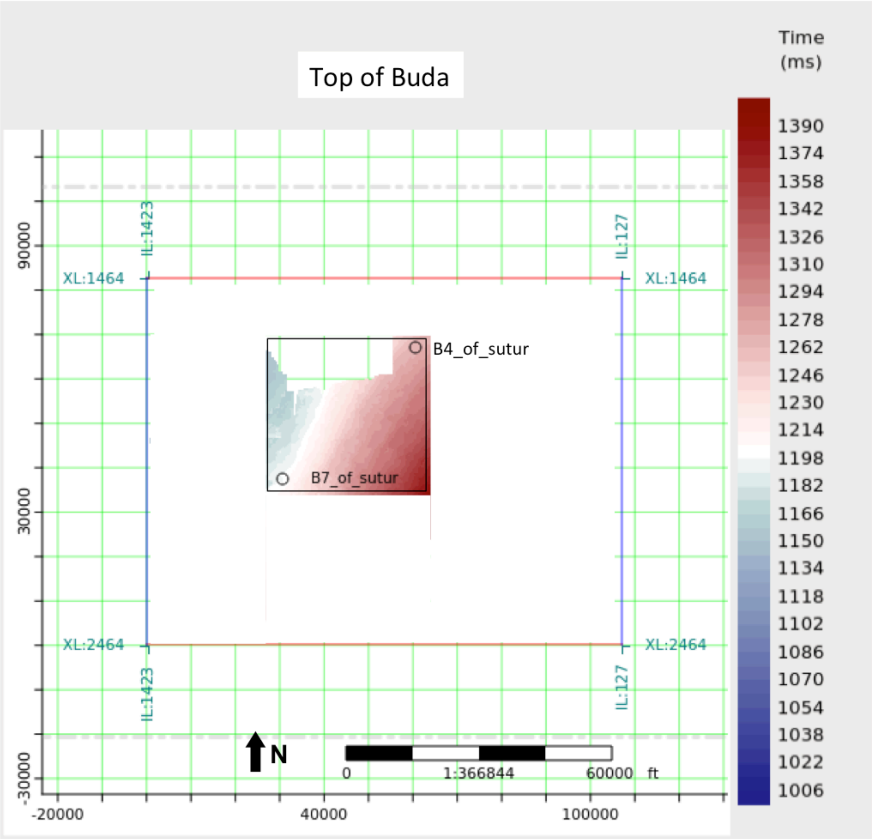

Figure 2.4: Map of the seismic survey in the inversion area, which is a subsection of the entire seismic survey. The color represents the Buda horizon depth in two way travel time (TWT). This inversion window contains 370 inlines and 381 crosslines. There are two wells in the survey area: B4 (B4_of_sutur) and B7 (B7_of_sutur).

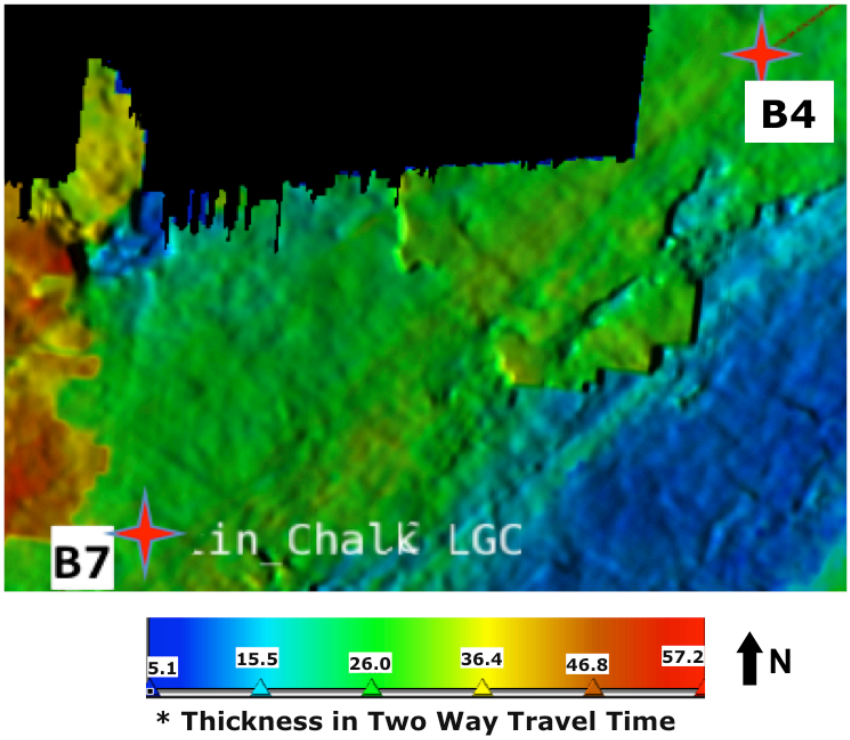

Figure 2.5: Eagle Ford Shale thickness in two-way-travel time (TWT), including both the Upper and Lower Eagle Ford. Red stars point out the location of well B4 and B7.

Figure 2.6 shows the post-stack seismic data for a single inline (IL) section. The inserted log is P-impedance from well B4. Two blue lines are the horizons corresponding to the top of the Eagle Ford Shale and top of the Buda Limestone. These horizons were picked based on post-stack seismic amplitude data. The tops of the Austin Chalk, Upper Eagle Ford, and Buda are clear enough to identify on post-stack seismic data, but it is difficult to identify the top of Lower Eagle Ford. The horizons of the tops of the Austin Chalk, Upper Eagle Ford, and Buda were used as guides and constraints for building the geostatistical model in Chapter 4. The uncertainty of the picked horizons will propagate to the geostatistical model and eventually influence the inverted stiffness. However, there is no quantitative way to calculate the final influence of the picked horizons on inverted stiffness; both the seismic data and the prior model control the inversion.

Figure 2.6 shows data only from 1200ms to 1320ms in TWT, but the inversion window also includes the Austin Chalk Formation above the Eagle Ford. Due to data confidentiality issues, the data in the Austin Chalk section is not shown. The top Buda is the interface that has the largest reflection amplitude in the study area. The impedance contrast between the Eagle Ford and the Buda is so large that it cannot be properly reconstructed using conventional inversion algorithms. Reconstructing the large impedance contrast between the Eagle Ford and Buda is one objective of the seismic inversion in this project. The top of the Eagle Ford has a small impedance contrast between Austin Chalk and Eagle Ford. Inside the Austin Chalk, there is another strong reflection, which is partially shown in Figure 2.6 (Xline 1600 – 1750). Using a deterministic inversion, it is difficult to identify this interface and the top of the Eagle Ford. However, using the inversion method I present in Chapter 4, these two interfaces are clearly identified.

The pre-stack seismic data is in the offset domain, but the seismic inversion is performed in the domain of incident angle. I transferred the pre-stack seismic data from the offset domain to the angle domain using the Straight Ray Method and root-mean-square (RMS) velocity model (Figure 2.7). The straight ray conversion equation is

$$\tan\boldsymbol{\theta} = \frac{\boldsymbol{X}}{\boldsymbol{V t_0}}, \tag{2.1}$$

where X is the offset, V is the RMS velocity, and t_0 is the total zero-offset travel time. Based on the conversion equation, and the RMS velocity model provided, the pre-stack seismic data is converted from the offset domain (X) to angle domain ($\boldsymbol{\theta}$). The velocity model in Figure 2.7 is a time migration velocity provided by the sponsor. I generate angle gathers (Figure 2.8) ranging from 4 to 42 degrees with 6 traces each. I used the angle range 4 – 36 for seismic inversion in Chapter 4. Again, based on the contract with the data owner, I am not allowed to show data in Austin Chalk. The wavelets used for inversion are angle-dependent statistical wavelets extracted from the seismic data, using deconvolution. Deconvolution is the process of filtering a trace to transform the wavelet of that trace into a form closer to the original wavelet. The filter used in the statistical wavelet extraction is the Wiener-Levinson Shaping filter, which is described by Equation 2.2

$$Ff = g\ . \tag{2.2}$$

where F is the autocorrelation of input seismic data, f is the desired filter, and g is the cross-correlation between the input seismic data and the desired output. The desired output is often a spike. A 90-degree phase shift is applied on the wavelets in order to match the wavelet phase. The wavelet amplitude spectrum is shown in Figure 2.9. The frequency range is about 10 – 50hz.

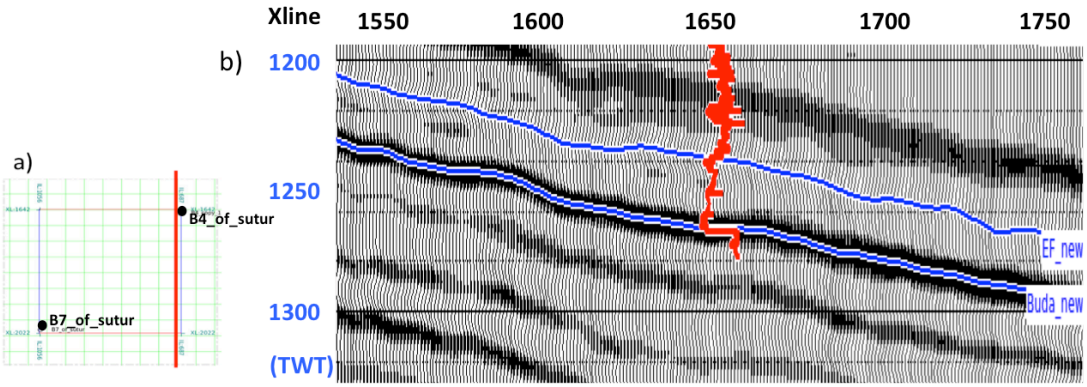

Figure 2.6: (a) The locations of Well B4, Well B7, and the seismic volume for inversion. Well B4 locates at the northeast corner of the inversion area, and well B7 locates at the southwest corner. (b) The PP data from the 2D slice from the red line in (a). The data is in TWT. The inserted curve is the P-wave impedance curve in Well B4. Blue horizontal lines are picked horizons corresponding to the top Eagle Ford and Buda.

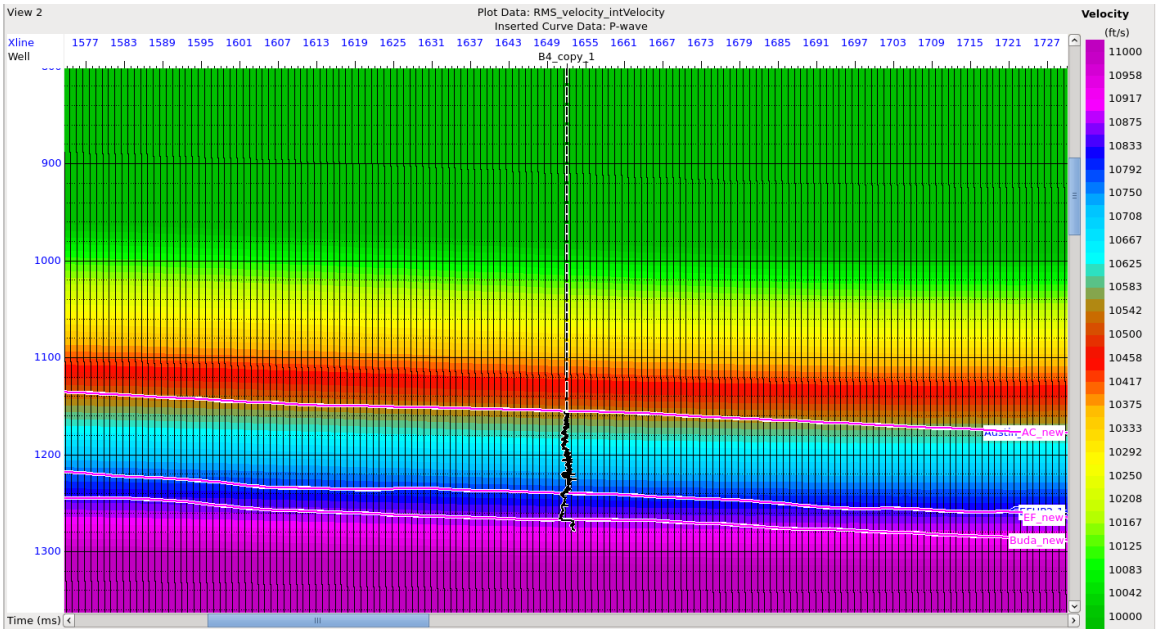

Figure 2.7: Velocity Model. This velocity model is a time migration velocity provided by the sponsor.

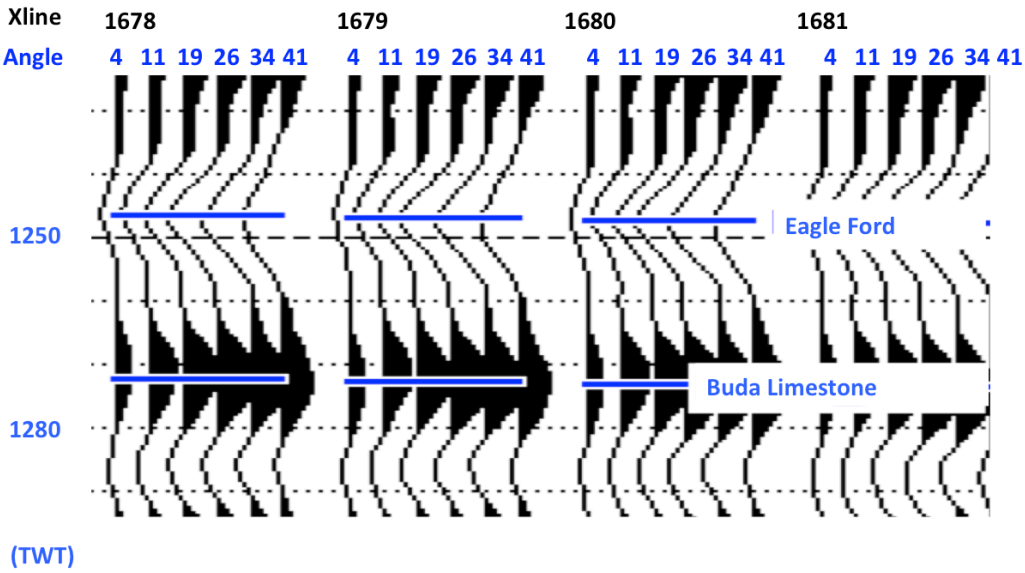

Figure 2.8: The P-P angle gathers from a 2D slice (red line in Figure 2.6a). The offset range is 4 – 41 degrees with 6 traces. The blue horizontal lines are picked horizons, the top Eagle Ford, and Buda. The interface between the Upper and Lower Eagle Ford cannot be resolved in the angle gathers.

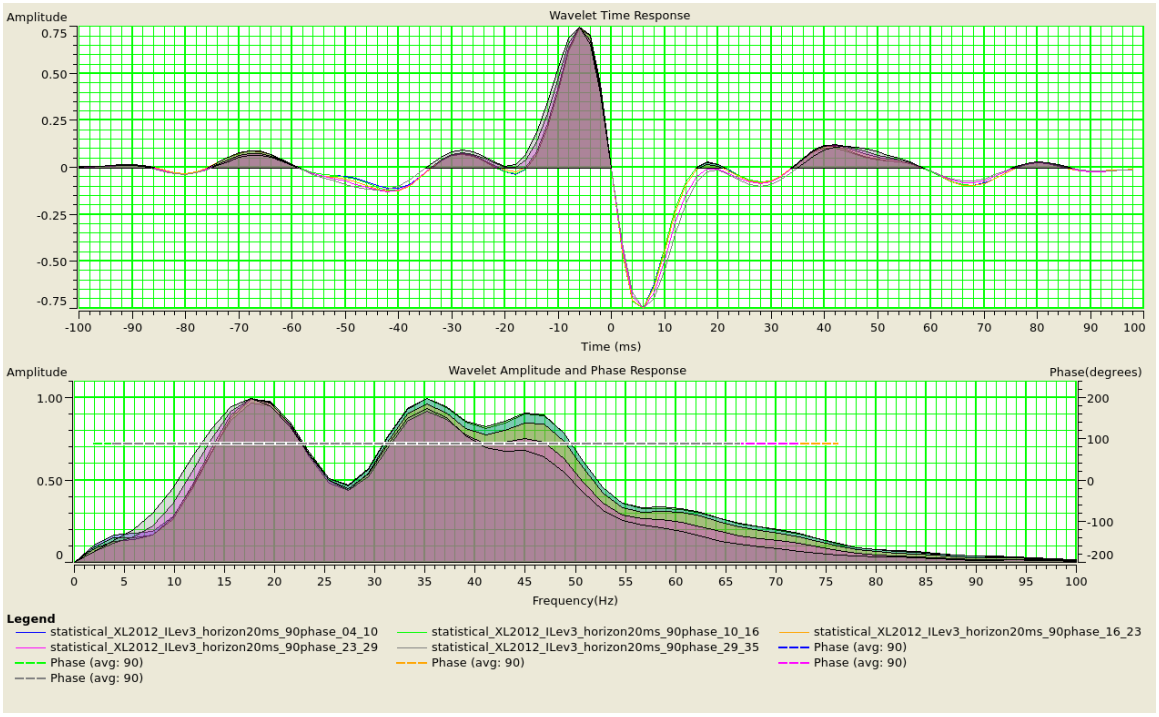

Figure 2.9: Angle-dependent wavelets extracted from the seismic data. The average phases of these wavelets are 90-degrees. The frequency range is about 10 – 50 Hz.

2.2.2 Well data

There are three wells used in this project. Wells B4 and B7 are within the seismic survey area, and well B5 is out of seismic coverage. Wells B4 and B7 are used to build the geostatistical prior models for seismic inversion; details for this part of work are explained in Chapter 4. For these two wells, the required logs are P- and S- impedance and density. Well B5 is used for rock physics modeling, as explained in Chapter 3. At the location of this well, the thickness of both the Lower and Upper Eagle Ford is about 700ft. I applied the rock physics modeling only on the Upper Eagle Ford; therefore, only the data from the Upper Eagle Ford is shown in this section.

Figure 2.10 shows the logs from well B4; from left to right are Gamma ray (GR), density, and P- and S- wave velocity. Based on a confidential agreement, I am not allowed to show data from the Austin Chalk, but logs in the Austin Chalk are used to build a geostatistical model for seismic inversion. Compared with the overlaying Austin Chalk and underlying Buda Limestone, the Eagle Ford has higher GR, lower density, and lower velocities. The Lower Eagle Ford at well B4 location is about 30ft thick with significantly higher GR and lower density, compared to the Upper Eagle Ford. The velocities of the Lower Eagle Ford are also lower than the Upper Eagle Ford. The large property contrasts between the Lower Eagle Ford and the Buda Limestone make the Buda horizon the highest amplitude event in the seismic data. One purpose of the seismic inversion is to reconstruct such a large property contrast. Figure 2.11 shows the logs of Well B7. At this location, the thickness of the Lower Eagle Ford is almost zero. Other measured petrophysical properties of well B7 are similar to those in Well B4.

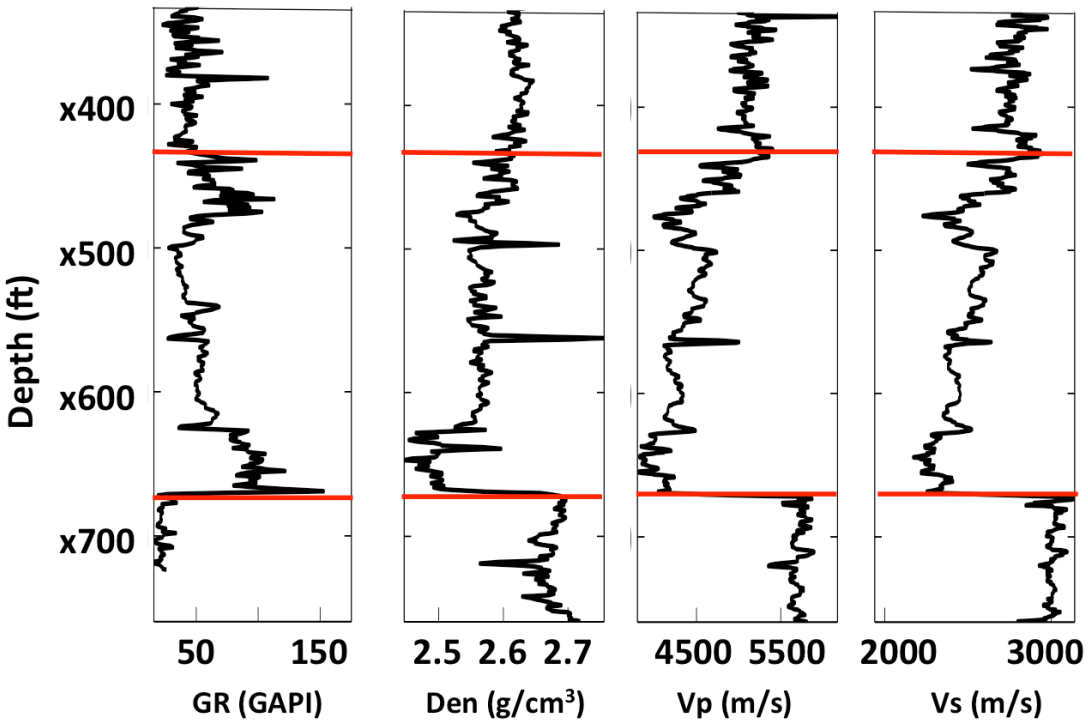

Figure 2.10: Log data from Well B4. From left to right, gamma ray, density, Vp, and Vs. The two red lines are the top and base of the Eagle Ford Shale. The formation above the Eagle Ford is the Austin Chalk and beneath it is the Buda Limestone. GR of the Eagle Ford Shale is higher than the Austin Chalk and Buda due to its high clay content, while Vp and Vs and density of the Eagle Ford Shale are lower than the other two formations. Around x650ft to x680ft the high GR of about 100 is a thin layer of the Lower Eagle Ford. Compared to the Upper Eagle Ford, the Lower Eagle Ford has higher GR, lower density and lower velocities because the Lower Eagle Ford has higher TOC content.

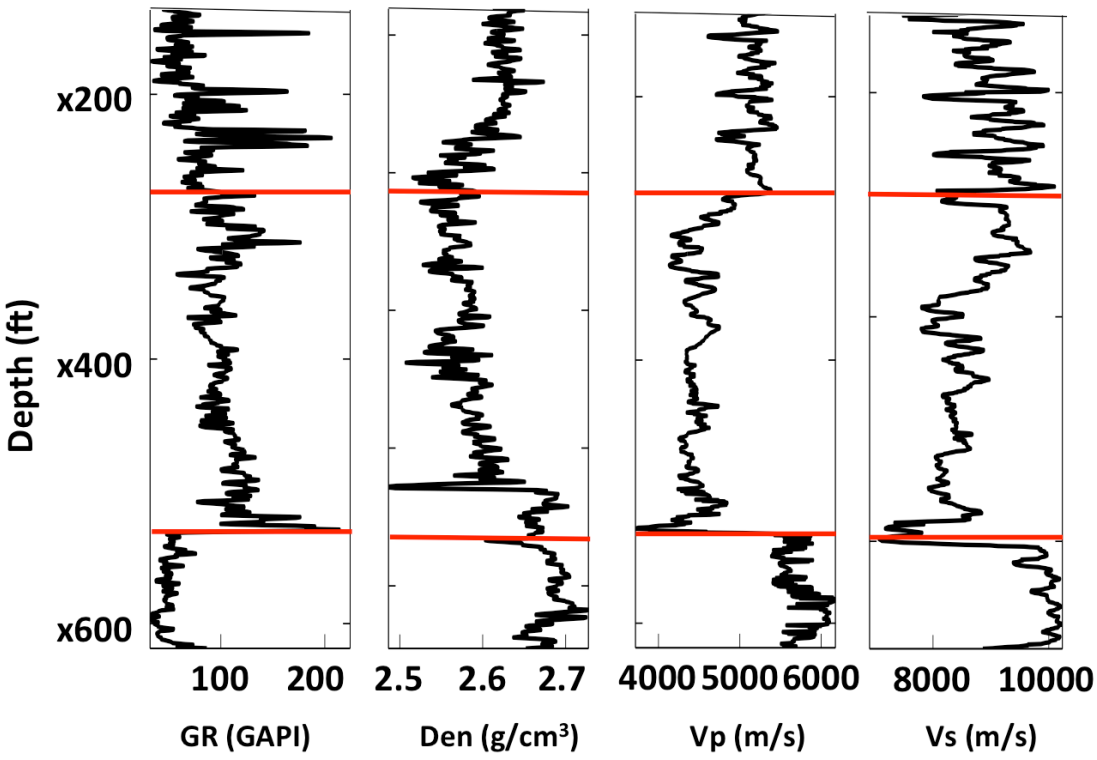

Figure 2.11: Log data from Well B7. From left to right, gamma ray, density, Vp, and Vs. The two red lines are the top and base of the Eagle Ford Shale. GR of the Eagle Ford Shale is higher than the Austin Chalk and Buda due to its high clay content, while Vp and Vs and density of the Eagle Ford Shale is lower than the other two formations. At this location, the thickness of the Lower Eagle Ford is almost zero.

Well B5 is the well used for rock physics modeling for the Upper Eagle Ford Shale. This well has a full suite of log measurements (Figure 2.12) including gamma rays, resistivity, density, neutron porosity, photoelectric factor and sonic logs; it also contains the porosity log, water saturation log, and lithology log (Figure 2.13) estimated from petrophysical inversion (Heidari and Torres-Verdin, 2013).

The petro-physical model assumed here is that the organic shale is composed of clay minerals, non-clay minerals, kerogen, hydrocarbon, and water. We use vector $\boldsymbol{X}$ to represent the composition as $\boldsymbol{X} = [C_1, C_2, \dots, C_n, C_k, \emptyset_t, S_w]^T$, where C_i represents the volume portion of i-th mineral, C_k represents the volume portion of kerogen, $\emptyset_t$ represents total porosity, and S_w represents water saturation. $\boldsymbol{X}$ is subject to $0 \leq X_i \leq 1$, and $\sum_1^n C_i + C_k + \emptyset_t = 1$. The initial guess about the composition $\boldsymbol{X}_{\text{ini}}$ is obtained from X-ray diffraction data. With the guessed composition, we can model the petrophysical properties of the bed. The petrophysical properties include density, neutron migration length (correlated to neutron porosity), electrical conductivity (reciprocal of resistivity), photoelectric factor (PE), and thorium (Th), uranium (U), and potassium (K) volumetric/weight concentrations. We use $\boldsymbol{P}(\boldsymbol{X})$ to represent these properties modeled from composition $\boldsymbol{X}$, and use $\boldsymbol{P}_{\mathbf{m}}$ to represent the measured petrophysical properties. If the objective function:

$$\boldsymbol{C}(\mathbf{X}) = \|\boldsymbol{W}_d \cdot (\boldsymbol{P}(\boldsymbol{X}) - \boldsymbol{P}_m)\|_2^2 + \alpha^2 \|\boldsymbol{X}\|_2^2, \tag{2.3}$$

is small enough, then the composition $\boldsymbol{X}$ will be accepted. Otherwise the composition will be updated until the value of the objective function is acceptable. In the objective function (Eq. 2.2), $\boldsymbol{W}_d$ is the weighting matrix, and α is the regulation factor.

Figure 2.12 shows the measured petrophyscial properties. From left to right, gamma ray, resistivity, density, neutron porosity, photoelectric factor, sonic logs, potassium (K) concentration, and thorium (Th) and uranium (U) concentrations. The GR

is about 50 GAPI, which is compatible with well B4 and B7. Density decreases in this interval; the velocity is about 2.2 km/s for S-wave and 4 km/s for P-wave. Figure 2.13 is the inverted rock properties for upper Eagle Ford at well B4.

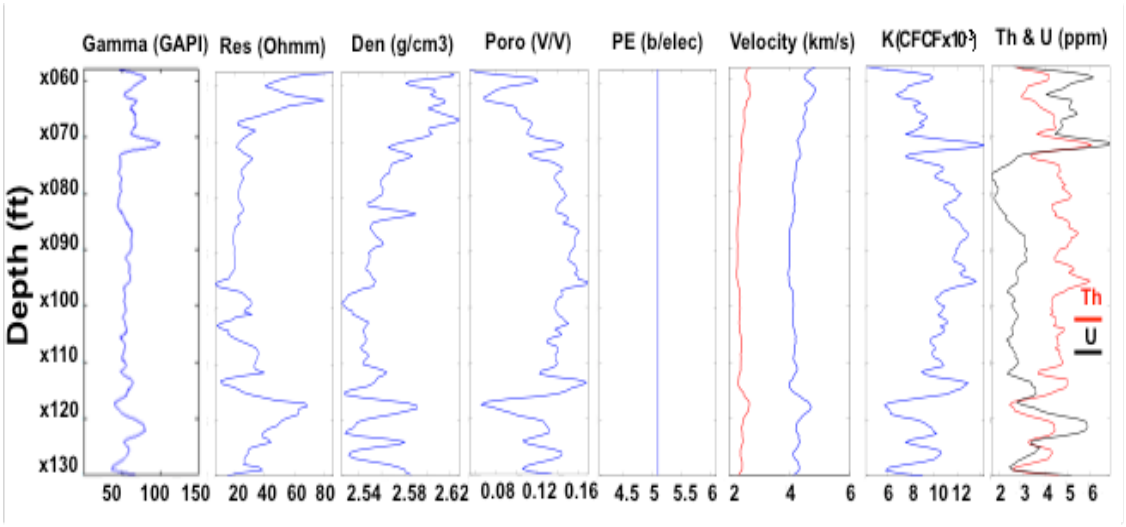

Figure 2.12: Measured log data within Upper Eagle Ford at well B5. (a) The measured petrophysical properties. From left to right are gamma ray, resistivity, density, neutron porosity, photoelectric factor, sonic logs, and potassium. These measured properties are the input for petrophysical inversion. (K) concentration, and thorium (Th) and uranium (U) concentrations.

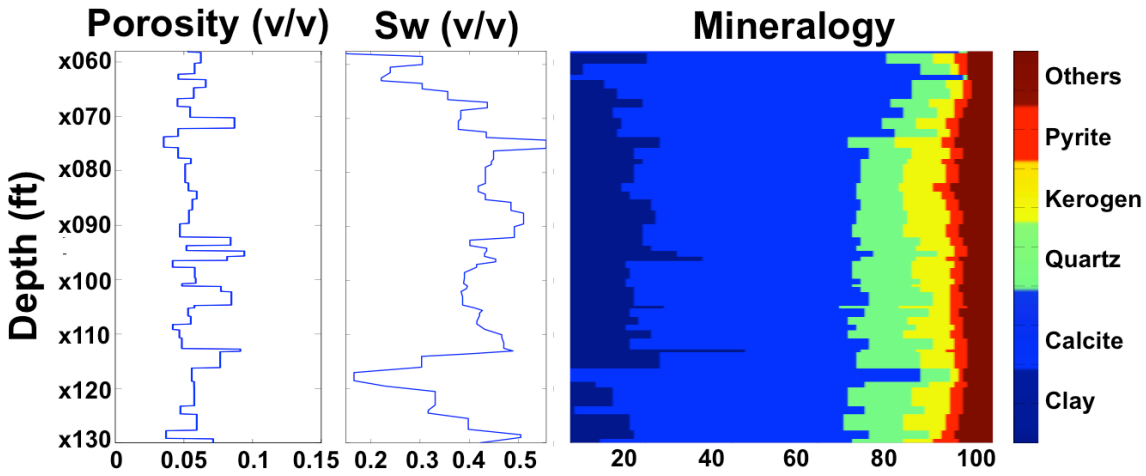

Figure 2.13: Petrophysically inverted composition. From left to right are porosity, water saturation, and lithology. Velocities are high at the top of this formation, corresponding to the high calcite volume. The decrease in velocities around x115ft corresponds to the increase in porosity, and the increase around x120ft corresponds to the increase of calcite volume. The major mineral components of the Upper Eagle Ford are calcite, clay, and quartz. The clay content variation is highly correlated with water saturation. The kerogen content varies from 0% to 13.1% volume concentration with an average at 7.9% in this interval. Approximately 2% by volume of pyrite is present, and other minor minerals are dolomite, plagioclase and K-feldspar.

The Upper Eagle Ford is a calcareous mudrock with major mineral components as calcite, clay and quartz. The organic matter, kerogen, varies from 0% to 13.1% in volume concentration with an average at 7.9% in this interval. There is about 2% volume concentration of pyrite, and other minor minerals are dolomite, plagioclase and K-feldspar. The porosity varies from 2.7% to 12% with an average at 6.4%. Analysis of these composition logs shows that the stiffness is correlated with clay content, and Kerogen content + porosity. In Chapter 3, I chose clay content and kerogen content + porosity as two influential independent parameters for rock physics modeling.

Well B5 provided the composition information needed in the rock physics modeling in Chapter 3. However, there are some other influential parameters in the rock physics modeling for which measurements are unavailable, for example, clay-cluster orientation patterns and pressure-dependent stiffness behaviors. The modeling uncertainty would reduce if there were additional datasets of X-ray diffraction measurements to estimate the clay cluster orientation and pressure-dependent stiffness measurements.

In Chapter 3, I will introduce the developed anisotropic rock physics modeling method and its application to the Upper Eagle Ford Shale using data from Well B5. Chapter 4 presents the geostatistics guided anisotropic seismic inversion method and its application on the seismic data shown in this chapter to resolve the thin Lower Eagle Ford Formation.

Chapter 3: Modeling the effects of micro-scale fabric complexity on the anisotropy of the Eagle Ford Shale

3.1 ABSTRACT

Micro-scale fabric influences the elastic properties of rock formations. The complexity of the micro-scale fabric of shale results from composition, platy clay minerals, kerogen, and their preferred orientation patterns. This micro-scale fabric is also the likely cause of the elastic anisotropy of the rock. In this paper, we present a comprehensive three-step rock-physics approach to model the anisotropic elastic properties of the Upper Eagle Ford Shale. We start with anisotropic differential effective medium modeling, followed by an orientation correction and then a pressure adjustment. This method accounts for the micro-scale fabric of the rock in terms of the complex composition, shape and alignment of clay minerals, pore space, and kerogen. In addition, we account for different pressure-dependent behaviors of P-waves and S-waves. The modeling provides anisotropic stiffnesses and pseudo logs of anisotropy parameters. The modeling results match log measurements relatively well. The clay content, kerogen content and porosity decrease the rock stiffness. The anisotropy increases with kerogen content, but the influence of clay content is more complex. Comparing the anisotropy parameter pseudo logs with clay content shows that clay content increases the anisotropy at small concentrations; however, the anisotropy stays constant, or even slightly decreases, as clay content continues to increase. This result suggests that the preferred orientation of clay clusters is preserved at low clay concentration but vanishes at high clay concentration. This method could also be applied to other shales with carefully chosen parameters to model anisotropic elastic properties.[1]

This chapter was published in Ren, Q. and K. T. Spikes, 2016, Modeling the effects of micro-scale fabric complexity on the anisotropy of the Eagle Ford Shale: Interpretation, 4, SE17 – SE29. The coauthor Spikes supervised the project.

3.2 INTRODUCTION

Characterizing unconventional resources from geophysical data is becoming increasingly important to improve economic recovery. To understand the geophysical responses of shales, we must understand how their microstructures influence their elastic responses. Micro-structural studies have demonstrated complex morphologies and fabrics (e.g., Chalmers et al., 2012; Sondergeld et al., 2010). In these two cases and in others, the complex fabric is likely the cause of the elastic anisotropy. This elastic anisotropy in turn controls seismic wave propagation and thus affects elastic wave amplitudes, travel times and ray paths (Banik, 1984, Sayers, 2005). As the link between rock properties and seismic responses, rock-physics models should account for the complex micro-scale fabric and resulting anisotropy.

Rock physics approaches have modeled the elastic properties of shales using various techniques. A popular approach has been through inclusion-based models. They have the flexibility to model the shapes of micro-scale grains and pore space by introducing aspect ratios of inclusions (Avseth et al., 2000). Examples of effective medium models are the self-consistent (SC) and differential effective medium (DEM) models (Norris, 1985; Berryman, 1992 and 1995; Mavko et al., 2009). Sayers and Den Boer (2011) applied the self-consistent method to deepwater subsalt Gulf of Mexico mudrocks and showed that the effective moduli varied as a function of different pore aspect ratios. The Jiang and Spikes (2013) study on the Haynesville Shale also showed that the pore aspect ratio had a strong influence on velocities. The work from Ren and Spikes (2014) on the Haynesville Shale with the anisotropic DEM method showed that grain aspect ratios, including that of clay and kerogen, and pore aspect ratios strongly affected both effective stiffness and anisotropy. Hornby et al. (1994) proposed an anisotropic effective medium model by aligning the inclusions in the horizontal plane to

build up an effective vertical transversely isotropic (VTI) medium. This method accounted for the complex shale composition and various grain shapes, but the platy clay minerals and clusters were fully aligned. However, the SEM images show that these clay minerals and clusters have different orientation directions. Bandyopadhyay (2009) used the DEM method to model the anisotropic elastic properties of the Bakken Shale. He showed that as the inclusion aspect ratio decreased, the effective stiffness components in the vertical direction decreased, whereas in the horizontal direction they increased; therefore, the anisotropy increased. Vasin et al. (2013) quantified the grain and pore shapes of the Kimmeridge shale from SEM and TEM images. The histogram of pore shapes indicated a significant number of both high aspect ratio (0.5–1) and low aspect pores (0.01–0.03). They modeled how these two types of pores influence the shale stiffness, using the GeoMIXself (GMS) approximation (Matthies et al., 2001). The GMS added elements of the geometric mean approximation to the self-consistent scheme. This method can describe the elastic properties of porous polycrystalline graphite and biotite gneiss. The results showed that adding high aspect ratio pores decreased all stiffness components but did not influence anisotropy. To the contrary, the low aspect ratio pores influenced both stiffness components and anisotropy. Research on the Muderong Shale (Kanitpanyacharoen et al., 2014) showed results similar to that of Vasin et al. (2013).

A rock-physics method for shale should be able to model the complex micro-scale fabric and anisotropy. More specifically, it should have the ability to model complex composition, various shapes of grains and pores, and various orientation distributions of the constituents. To accomplish this, the model should be anisotropic but coupled with an orientation distribution function (ODF) that describes the degree of alignment of grains and pores. Accordingly we developed an anisotropic rock-physics model that accounts for complex composition, shape and alignment of clay minerals, pore space, and kerogen,

followed by pressure-dependent behaviors of P- and S-waves. We applied this multi-step technique to the Upper Eagle Ford Shale and mapped the rock properties to anisotropy parameters. The results show that clay, kerogen, and porosity strongly influence the stiffness and anisotropy of the rock. The kerogen content increases anisotropy. Computed pseudo logs of anisotropy parameters show that the anisotropy correlates with clay volume at relatively low clay concentration but anisotropy does not increase with clay at relatively high clay concentration.

Relationships among anisotropy, composition and alignment

Seismic velocity measurements in the laboratory indicate that shale exhibits VTI symmetry, with the symmetry axis perpendicular to bedding direction (e,g., Vernik and Nur, 1992, Hornby, 1998, Dewhurst and Siggins, 2006, Jones and Wang, 1981, and Wang, 2002). This anisotropy relates to the complex fabric through (a) alignment of platy clay minerals, (b) alignment of clusters of clay minerals, (c) alignment of non-spherical pores and microcracks, (d) alignment of fractures, (e) fine-scale laminations of shaly materials with different stiffnesses, and (f) lenses of kerogen (Vernik and Liu, 1997). Each of these might play a role in the effective anisotropy. Our model accounts for each of these options except the alignment of fractures, and we focus on the contributions of clay and kerogen and their orientations.

Many studies have been performed to understand how clay and kerogen contribute to the elastic anisotropy. Vernik and Milovac (2011) investigated the anisotropy of organic shale using core measurements, logging data, and heuristic models. The results showed that kerogen, porosity, and clay content controlled the elastic properties of organic shale. The velocity anisotropy mainly came from kerogen and the clay minerals with the preferred orientation parallel to the bedding plane. Vernik and Liu

(1997), based on various datasets consisting of low porosity black shale, showed that the Thomsen (1986) parameter epsilon increased with kerogen volume up to about 40%. However, Allan et al. (2014) showed that the contribution of kerogen to anisotropy was masked by clay when the shale contained high clay content (> 40%) and showed a high degree of clay mineral alignment. Johnston and Christensen (1995) investigated the relationship between the preferred orientation of clay minerals and the anisotropy for Devonian-Mississippian black shale formations, using laboratory velocity measurements, X-ray diffraction techniques, and electron microprobe backscatter imaging. Their research showed a strong positive correlation between the degree of preferred clay orientation and seismic anisotropy. Allan et al. (2014) studied the correlation between P-wave anisotropy and both clay content and clay alignment of five mature organic rich shale samples. They used X-ray diffraction techniques (Wenk et al., 2008) to quantify the amount of clay minerals and capture their orientation distributions. The velocity anisotropy was obtained from directional velocity measurements in the laboratory. This research suggested that the alignment of anisotropic clay species, rather than the volume of clay minerals, influenced the anisotropy. The contribution of clay to anisotropy for clay-rich shale would drop to zero when all the clay minerals were randomly oriented, according to their research.

Additional complexity exists because alignments of clay minerals are not always present in shale formations. Scanning electron microscopy (SEM) images and backscattered electron (BSE) images from various shales (Sone, 2012; Hornby et al., 1994; Vernik and Milovac, 2011) commonly show aggregates of aligned clay minerals. At the core scale, these locally aggregated clay mineral clusters might have different preferred orientation directions; therefore, the preferred orientation might vanish at the core scale. As a result, the clay mineral clusters no longer contribute to the anisotropy of

the rock (Sone, 2012). Figure 3.1 shows an SEM image from the Eagle Ford Shale, which reveals the variation of orientation direction of clay mineral clusters. The yellow circles in Figure 3.1 highlight the clay mineral clusters with different preferred orientations. Although the clay minerals within a cluster share an apparent similar direction, the preferred orientation differs among clusters. This difference reduces the degree of alignment of clay minerals at a larger scale and decreases their contributions to the effective anisotropy. Johansen et al. (2004) demonstrated numerically that the preferred orientation patterns of non-spherical grains strongly influence the elastic properties and anisotropy of shale. They evaluated how the orientation influenced the anisotropy using various orientation distribution models. The results showed that the higher the degree of alignment of grains corresponded to higher anisotropy. We incorporate this micro-scale orientation information into the rock-physics modeling through orientation distribution functions.

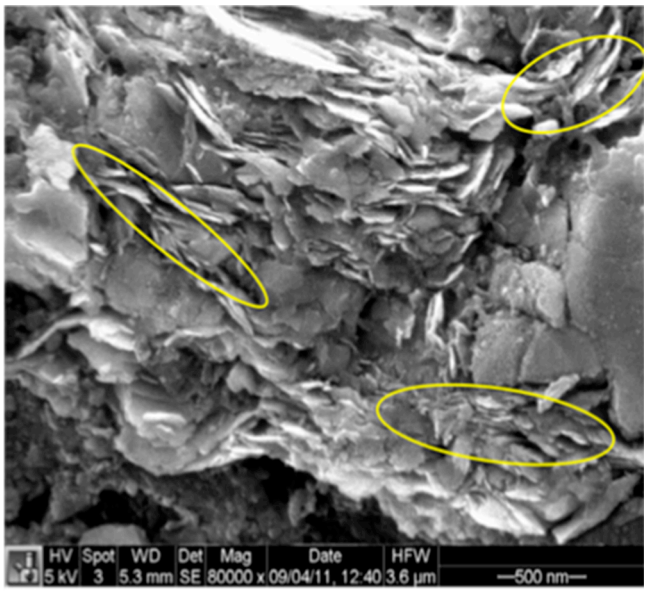

Figure 3.1: SEM image from the Eagle Ford Shale (Sone, 2012). The yellow circles point out the clay clusters with different orientation directions.

3.3 METHODOLOGY

The anisotropic rock-physics method presented in this paper contains three parts: the anisotropic DEM modeling, orientation correction, and pressure adjustment. In this section, we discuss the details of these steps.

3.3.1 Anisotropic DEM

The DEM method models two-phase composites by adding one phase (phase 2) as a series of inclusions with specified shapes and stiffnesses to the matrix phase (phase 1). The combined two-phase effective medium is considered as the new matrix phase for further mixing. The anisotropic effective stiffness (Equation 3.1) is determined by a tensor (Hornby et al., 1994):

$$\frac{d}{dv}\left(c^{\widetilde{DEM}}(v)\right) = \frac{1}{(1-v)}\left(c^{i} - c^{\widetilde{DEM}}(v)\right)\times\left[I + \tilde{G}\left(\tilde{c}^{i} - c^{\widetilde{DEM}}(v)\right)\right]^{-1}. \quad (3.1)$$

In (Equation 2), $\widetilde{c^{DEM}}$ is the effective stiffness of the entire rock, $\tilde{c}^{i}$ is the stiffness of i-th inclusion, ν is the volume portion of the i-th inclusion respect to the entire rock, and $\tilde{G}$ is the geometry factor containing inclusion shape information. The output is a VTI stiffness tensor, $\widetilde{c^{DEM}}$, with 5 independent components, which are $c_{11}, c_{33}, c_{44}, c_{66}$, and c_{13}.

The DEM method assumes that all inclusions are fully aligned in the horizontal plane. The anisotropy comes from the alignment of non-spherical inclusions. The resulting error from fully aligned inclusions is corrected in the orientation correction in the next step. A previous study (Ren and Spikes, 2014) showed that the inclusion aspect ratio strongly affected both effective stiffness and anisotropy in this anisotropic DEM method. In the study, we used distributions of inclusion aspect ratios for clay, kerogen,

and pore space to account for the micro-scale complexity of grain shapes. The aspect ratio of each inclusion was drawn from a normal distribution with a given mean value. The mean value of each aspect ratio distribution was obtained from a series of numerical experiments. Comparing the modeled to the measured stiffnesses identified the best fit mean aspect ratios.

3.3.2 Orientation Correction

After constructing the effective VTI medium, the next step is the orientation correction to compensate for the effect of fully aligned inclusions. Laboratory measurements or empirical models can provide orientation distribution functions (ODF) for rock-physics modeling. Measurement-based methods include high-resolution X-ray texture goniometry (Ho et al., 1995, 1996, 1999, Aplin, 2006). This technique identifies the presence of clay mineral phases by a "2θ scan" and determines the degree of preferred orientation of the existing clay mineral phases by a "pole-figure scan". A more comprehensive method is based on the synchrontron X-ray diffraction technique (Wenk et al., 2008, Kanitpanyacharoen et al., 2011). This method measures the preferred orientation patterns by 3D X-ray diffraction imaging as a function of the Bragg angle and azimuth. When none of the above measurements are available, the ODFs can be constructed either from statistical models or a compaction model. The statistical models define the alignment as a distribution spreading around a mean value, for example a Gaussian distribution. The compaction model describes the ODF as a result from vertical compaction of sediment. Johansen et al. (2004) reviewed and compared these different models in terms of calculated Legendre coefficients. Their study showed that all the statistical models generated almost identical Legendre coefficients, and the results from compaction models were only slightly different from those using statistical models.

Legendre coefficients are calculated from expanding an ODF into generalized spherical harmonics (Roe, 1965). Sayers (1994) gave formulas for computing the effective stiffness of transversely isotropic media from the stiffness modeled with fully aligned inclusions and the Legendre coefficients.

The compaction-model ODF we use in this disseration is defined as

$$W(\xi) = \frac{1}{8\pi^2}\frac{a^2}{(\xi^2+(1-\xi^2)a^2)^{3/2}}, \tag{3.2}$$

where a is the compaction factor, and ξ is the cosine of bedding direction with respect to the horizontal plane (Owens 1973; Baker, Chawla and Krisek 1993). The Legendre coefficients are calculated based on the ODF as:

$$W_{200} = \frac{1}{4\sqrt{2}\pi^2}, \tag{3.3}$$

$$W_{200} = \sqrt{\frac{5}{2}}\int_{-1}^{1} W(\xi)\, P_2(\xi) d\xi, \tag{3.4}$$

$$W_{400} = \sqrt{\frac{9}{2}}\int_{-1}^{1} W(\xi)\, P_4(\xi) d\xi, \tag{3.5}$$

where the $P_l(\xi)$ are the Legendre polynomials of order l.

$$P_2(\xi) = \frac{1}{2}(3\xi^2 - 1), \tag{3.6}$$

$$P_4(\xi) = \frac{1}{8}(35\xi^4 - 30\xi^2 + 3). \tag{3.7}$$

Here we account for the Legendre coefficients W_{lmn} with $l \leq 4$ because stiffness is a fourth-rank tensor (Morris, 1969, Sayers, 1994). For a transversely isotropic medium, the non-zero W_{lmn} only occurs with even l and m, and $n = 0$. In addition, for a VTI medium, m equals zero as well. Following Sayers's (1994) procedure, Johansen et al. (2004) showed that the corrected stiffness could be calculated as:

$$C_{corrected} = [T_{000} + W_{200}^N T_{200} + W_{400}^N T_{400}]C_{align}, \tag{3.8}$$

W_{200}^N and W_{400}^N are normalized Legendre coefficients, C_{align} are the modeled stiffness with fully aligned inclusions, and $T_{\mathrm{i}00}$ are constant matrices as:

$$T_{000} = \frac{1}{15}\begin{bmatrix} 8 & 3 & 4 & 8 & 0 \\ 8 & 3 & 4 & 8 & 0 \\ 6 & 1 & 8 & -4 & -10 \\ 1 & 1 & -2 & 6 & 5 \\ 1 & 1 & -2 & 6 & 5 \end{bmatrix} \tag{3.9}$$

$$T_{200} = \frac{1}{21}\begin{bmatrix} 8 & -6 & -2 & -4 & 0 \\ -16 & 12 & 4 & 8 & 0 \\ -6 & 1 & 5 & -4 & 14 \\ 1 & 1 & -2 & 3 & -7 \\ -2 & -2 & 4 & -6 & 14 \end{bmatrix} \tag{3.10}$$

$$T_{400} = \frac{1}{35}\begin{bmatrix} 3 & 3 & -6 & -12 & 0 \\ 8 & 8 & -16 & -32 & 0 \\ -4 & -4 & 8 & 16 & 0 \\ -4 & -4 & 8 & 16 & 0 \\ 1 & 1 & -2 & -4 & 0 \end{bmatrix} \tag{3.11}$$

3.3.3 Pressure Adjustment

In addition to the micro-scale fabric, pressure is another influential factor on elastic properties and anisotropy. Sone and Zoback (2013) measured the directional-dependent velocities corresponding to stiffnesses (c_{11}, c_{33}, c_{44}, and c_{66}) of the Eagle Ford Shale under different effective pressures. The measured data are presented in Figure 3.2. As shown in Figure 3.2, the four stiffness components are all pressure dependent. However, the pressure-dependent behaviors are different among c_{11}, c_{33} (Figure 3.2a), which correspond to compressional wave, and c_{66}, c_{44} (Figure 3.2b), which correspond to shear waves. Figure 3a explains the difference between compressional wave and shear

wave dependence on pressure. These different pressure-dependent behaviors could relate to the pores that close as effective pressure increases. As pressure increases, the pore space with low aspect ratio closes; the pore space with high aspect ratio remains open. Therefore, one response of rock to the increase of pressure is the closure of flat pore space. We modeled the response of c_{11}/c_{66} and c_{33}/c_{44} with respect to the increase of pore aspect ratio, as shown in Figure 3.2.13. As the pore aspect ratio increases, the stiffness ratios increase. This observation agrees with measurements in Figure 3.2.12 in that as the effective pressure increases, the ratio of compressional to shear stiffness increases. Because the P- and S-waves respond differently to pressure, the anisotropic P-wave and S-wave velocity data cannot both be modeled correctly without accounting for the pressure effect. In this study, we modeled c_{33} and c_{11} to match the log data by anisotropic DEM and orientation correction, and then we applied pressure correction on c_{44} and c_{66}. We used the difference of c_{11}/c_{66} and c_{33}/c_{44} between in situ (41Mpa) and reference effective pressure (5Mpa) to adjust the modeled shear stiffness components. The reference effective pressure is the assumed model pressure for effective medium modeling. The value of reference effective pressure affects the pressure adjustment; however, we do not know the exact value. The 5Mpa reference effective pressure was chosen based on multiple tests. The adjusted shear stiffness components are:

$$c_{44\_adjusted} = \frac{c_{33\_DEM}}{(c_{33}/c_{44})_{DEM}+\Delta(c_{33}/c_{44})}, \tag{3.12}$$

and

$$c_{66\_adjusted} = \frac{c_{11\_DEM}}{(c_{11}/c_{66})_{DEM}+\Delta(c_{11}/c_{66})}, \tag{3.13}$$

where $\Delta(c_{33}/c_{44})$ and $\Delta(c_{11}/c_{66})$ are the differences of each respective ratio between in situ and low measured effective pressure. The subscript *DEM* refers to the results from the orientation correction. This pressure correction is applied only to the c_{44} and c_{66} terms.

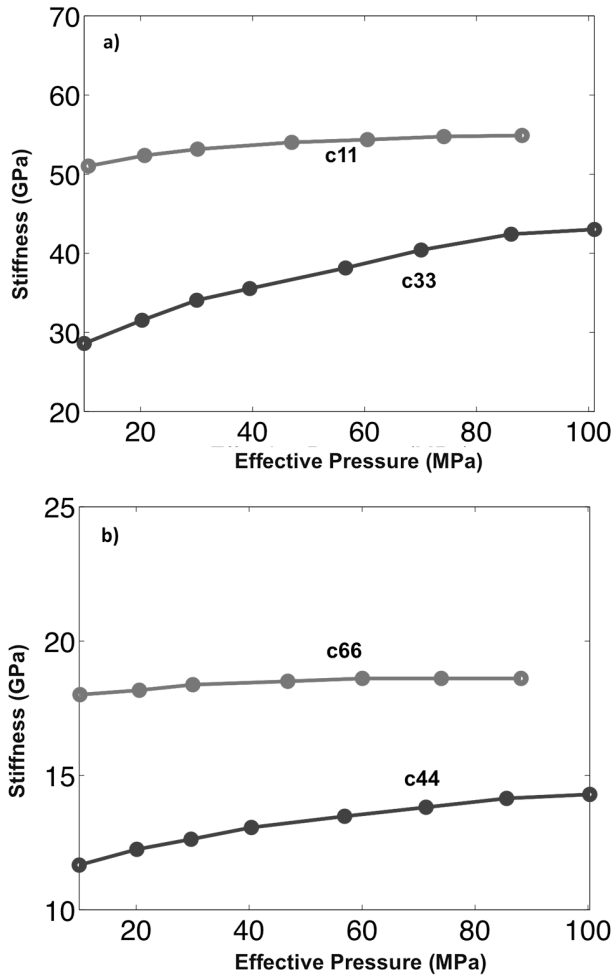

Figure 3.2: Pressure dependence of the dynamic moduli (a) c_{11} and c_{33}, (b) c_{44} and c_{66} of the Eagle Ford Shale. Data are from Sone and Zoback (2013). The c_{11} and c_{33} correspond to the horizontally and vertically propagating compressional waves, respectively, whereas c_{44} and c_{66} correspond to the horizontally and vertically propagating horizontally polarized shear waves, respectively. All four stiffness components increase with effective pressure at low effective pressure and tend to flatten at high effective pressure. However, the pressure-dependent behaviors of these four stiffness components are different.

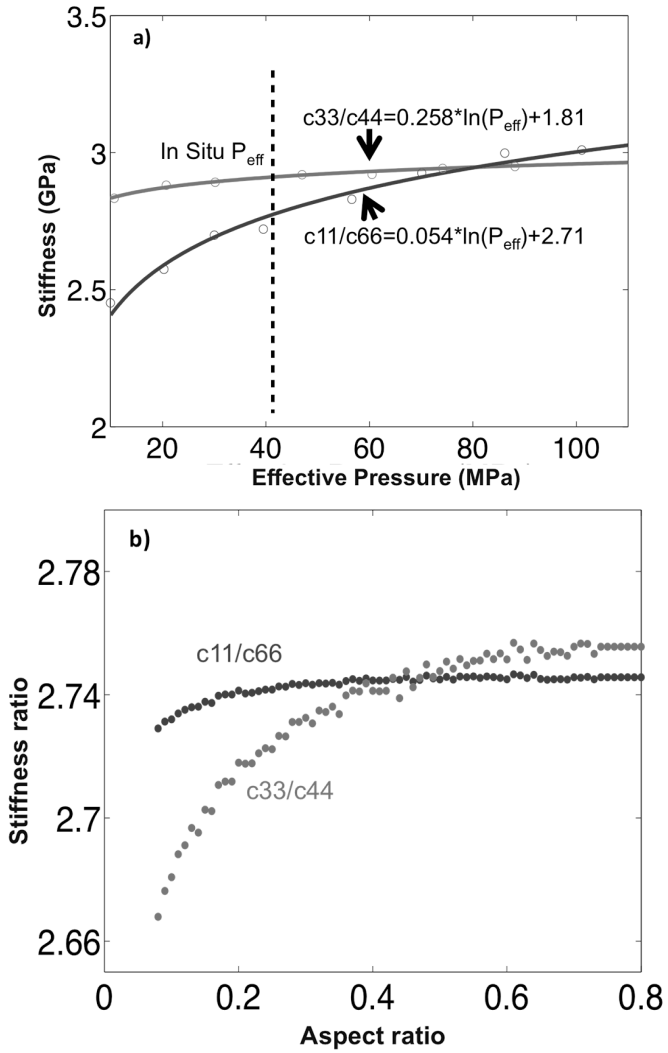

Figure 3.3: (a) Pressure dependence of the stiffness component ratios c_{11}/c_{66} in blue, and c_{33}/c_{44} in red. The points are calculated from the measurements from Sone and Zoback (2013), and the two lines are fitted exponential curves. The in situ effective pressure of Eagle Ford Shale is about 41Mpa. The difference of c_{11}/c_{66} and c_{33}/c_{44} between in situ and low effective pressure (about 5Mpa) was calculated from the fitted curve. (b) Pore aspect ratio dependence of c_{33}/c_{44} (red) and c_{11}/c_{66} (blue). As the aspect ratio increases from 0.1 to 0.8, both c_{33}/c_{44} and c_{11}/c_{66} increase and then go to flatten. In this modeling, we only changed the pore aspect ratio, but we did not reduce the porosity.

3.4 APPLICATION TO THE UPPER EAGLE FORD

3.4.1 Study Area and Data

The Upper Cretaceous Eagle Ford Shale is located in the Maverick Basin and the adjacent San Marcos Arch in south Texas. It extends farther northeastward to the East Texas Basin (Hentz, 2010). The Eagle Ford Shale is overlain by the Austin Chalk and underlain by the Buda Limestone. The Eagle Ford Shale contains both Upper and Lower intervals, and we focus on the Upper Eagle Ford.

The Upper Eagle Ford is a calcareous mudrock with major mineral components that include calcite, clay and quartz. This study contains one well, whose log panel is shown in Figure 3.2.12 and 2.13. Figure 3.2.12 shows the petrophysical properties from the well. From left to right are gamma ray, resistivity, density, neutron porosity, photoelectric factor, sonic logs, potassium (K) concentration, and thorium (Th) and uranium (U) concentrations. The middle part of the formation has constant relatively low resistivity, density, velocity, uranium concentration and relatively high neutron porosity and potassium concentration. The properties in the upper and lower part of this formation fluctuate. Figure 3.2.13 shows the porosity log, water saturation log, and mineralogy logs. These composition logs were estimated from a petrophysical inversion algorithm (Heidari and Torres-Verdin, 2013), which is explained in Chapter 2. The composition logs show that the kerogen content varies from 0% to 13.1% volume concentration with an average at 7.9% in this interval. Approximately 2% by volume of pyrite is present, and other minor minerals are dolomite, plagioclase and K-feldspar. The porosity varies from 2.7% to 12% with an average at 6.4%. The porosity changes from high to low at round 9115ft corresponding to the velocity variation.

Sone and Zoback (2013) measured the directional-dependent velocities corresponding to stiffnesses (c_{11}, c_{33}, c_{44}, and c_{66}) of the Eagle Ford Shale under

different effective pressures. The measured data are presented in Figure 3.2. Cores from which these measurements were obtained are not from the well used in this work, but the velocities measurements are applied in this work. The four stiffness components are all pressure dependent, but the pressure-dependent behaviors are different among compressional (Figure 3.2a) and shear (Figure 3.2b) stiffness components. Figure 3.3a shows the pressure-dependent ratios c_{11}/c_{66} and c_{33}/c_{44}, which are the ratios of compressional and shear stiffness components in the horizontal and vertical directions, respectively. Exponential curves were fitted to the ratios.

3.4.2 Modeling Result

We modeled how rock stiffness changes with porosity and kerogen volume, using the three-step rock-physics method. To reduce the model parameter space, we used the average volume concentration within the Upper Eagle Ford for calcite, quartz, pyrite, dolomite, plagioclase, K-feldspar, and average fluid saturation in the rock-physics modeling. The volume of a mineral refers to the volume portion of the mineral with respect to the entire rock. These average mineralogy volume concentrations come from the petrophysical inversion; the average fluid saturations are from available core measurements at several depths within the Upper Eagle Ford. These composition data are listed in Table 3.1. The volume ratio of kerogen and porosity was kept constant at 1.14, which is the average ratio in the well logs.

	Calcite (V/V)	Quartz (V/V)	Pyrite (V/V)	Dolomite (V/V)	K-feldspar (V/V)	Plagioclase (V/V)	Sw (V/V)	Sg (V/V)	So (V/V)
Upper EF	0.53	0.11	0.025	0.0064	0.0064	0.038	0.35	0.45	0.20

Table 3.1: Mineralogy, fluid of Upper Eagle Ford. (Reference to entire rock)

We used isotropic mineral and fluid stiffnesses, as listed in Table 3.2. The density of clay was calculated from the density log and composition logs by linear regression. The moduli and densities of minerals, other than clay density, were from Mavko et al. (2009); the values for kerogen and fluid came from (Heidari and Torres-Verdin, 2013). In the modeling, the mean aspect ratio was set to 0.15 for clay mineral, 0.1 for pore space, 0.1 for kerogen, and 1 for all other minerals. The size of each inclusion was modeled as a normal distribution with mean value of 0.05% by volume of the matrix rock. We first modeled the isotropic solid background using the DEM. The solid background included calcite, quartz, pyrite, dolomite, K-feldspar, and plagioclase. Then the non-spherical kerogen grains and the clay-fluid composites were added to the background using the anisotropic DEM method. The clay-fluid composites are the combination of clay minerals and fluid in the pore space. Fluid was added to clay minerals using anisotropic DEM modeling with an aspect ratio of 0.1; then the composites were added to the entire rock with aspect ratio at 0.15.

	Calcite	Clay	Quartz	Pyrite	Kerogen	Water	Gas	Oil	Dolomite	Orthoclase	Plagioclase
Density (g/cm3)	2.71	2.80	2.65	4.93	1.25	1.07	0.13	0.7	2.87	2.64	2.63
μ(GPa)	32	7	45	132.5	4	0	0	0	45	29.45	23.63
K (GPa)	73	21	36.6	1474	5	2.2	0.21	0.6	94.9	62.87	75.6

Table 3.2: Mineral and fluid properties used in the modeling.

Up to this point, all the non-spherical inclusions were fully aligned in the horizontal plane, establishing an effective VTI medium. The modeled anisotropy was as high as 0.7 for epsilon, which is much larger than the measured epsilon of 0.2 (data provided by the sponsor). The fully aligned inclusions caused this significant overestimation of modeled anisotropy. We applied the orientation distribution correction on this established effective VTI medium to compensate for the overestimated anisotropy. Equation 3 defines the ODF with the compaction factor set to 3, based on which the Legendre coefficients were calculated, and the corrected stiffness was modeled by equation 9. Finally, we used equation 13 and 14 to calculate the pressure-adjusted shear stiffness components. The calculated $\Delta(c_{33}/c_{44})$ equals 0.57, and $\Delta(c_{11}/c_{66})$ equals 0.12. In Figure 3.4, we show how the modeled c_{33} and c_{44} change through these three steps.

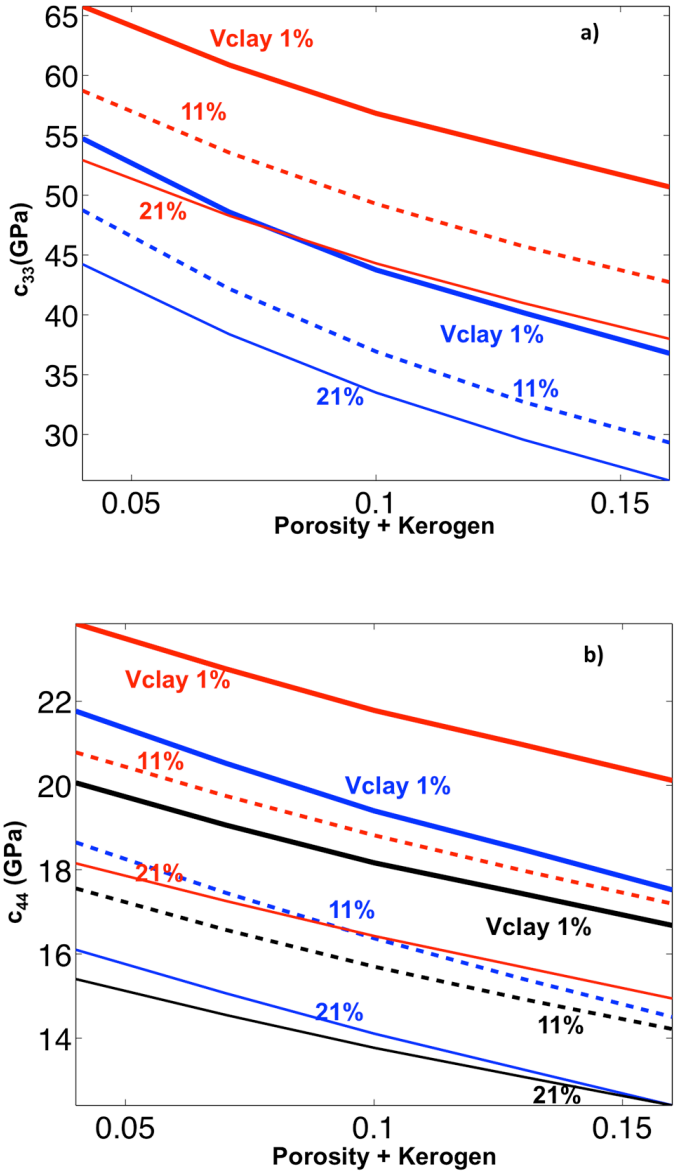

Figure 3.4: The change of modeled (a) c_{33}, and (b) c_{44} from step 1 to step 3. In both figures, each color represents the modeled stiffness components for a given step: step 1 (anisotropic DEM) results in blue, step 2 (orientation correction) results in red, and step 3 (pressure adjustment) results in black. The three lines in each color represent the increase of clay volume from 1% (thick solid lines) to 11% (dash lines), and 21% (thin solid lines), as from top to bottom. The orientation correction increased c_{33} and c_{44}; the pressure adjustment decreased c_{44}. The pressure adjustment is only applied to c_{44}, so there is no black line in (a).

Each value of modeled stiffness corresponded to a specific pair of modeled {clay volume, porosity plus kerogen volume}, and had associated values of modeled anisotropy parameters. On the other hand, the mineralogy logs provided the {clay volume, porosity plus kerogen volume} value at every measured depth. Comparing the measured {clay volume, porosity plus kerogen volume} pairs at each measured depth to the modeled values in a grid search, we obtained the corresponding modeled stiffness and modeled anisotropy parameters at that depth. Repeating this procedure for all the measured depths provided the modeled stiffness logs and modeled anisotropy parameter pseudo logs.

Modeled and measured stiffness components c_{33} and c_{44} are plotted as a function of porosity plus kerogen in Figure 3.6. The lines represent models for different modeled clay volumes, and the points are the log measurements in color of clay volume. Both the models and the log measurements show that c_{33} and c_{44} decrease as clay volume increases and as porosity plus kerogen increases. The measured points with relatively low clay volume are located in the upper left corner of these two figures; they match the model with 1% clay volume relatively well. Towards the lower right, the measured points show higher clay volume, and they match the models with higher clay volume as well. The models do not perfectly represent all the measured points, but they match fairly well. Figure 3.6 shows measured (calculated from measured velocity and density) and modeled stiffnesses as a function of depth. The closest match of modeled and measured pairs of {clay volume, porosity plus kerogen volume} were found for each depth sample. The corresponding stiffnesses are displayed in Figure 3.6, with c_{33} on the left and c_{44} on the right. The overall trends match for both stiffnesses.

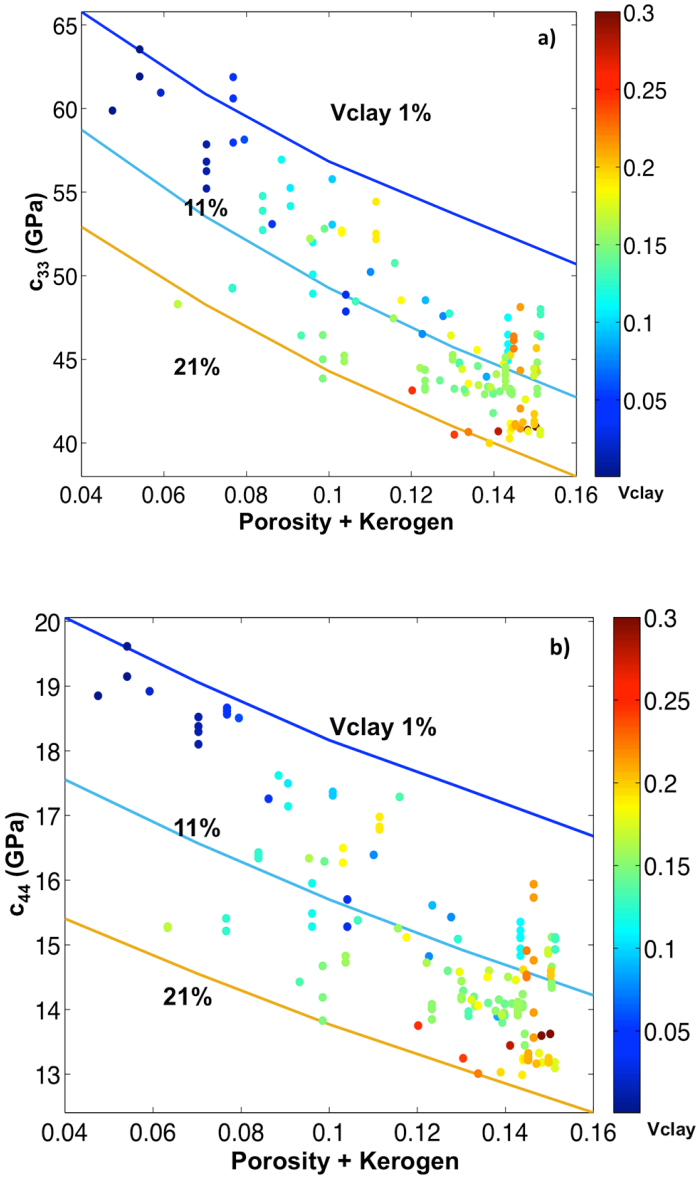

Figure 3.5: The modeled stiffness (a) c_{33} and (b) c_{44} as a function of porosity plus kerogen volume changing from 0.04 to 0.16. The lines represent stiffness models with different volumes of clay, whereas the points are calculated from log measurements (a) P-wave and (b) S-wave, colored by clay volume. The models with 1% clay volume match the measured point with low clay volume at upper left. Towards the lower right, the models with higher clay volume represent the measured points with higher clay volume. Although the models do not represent every measured point, the models follow the trends in the data.

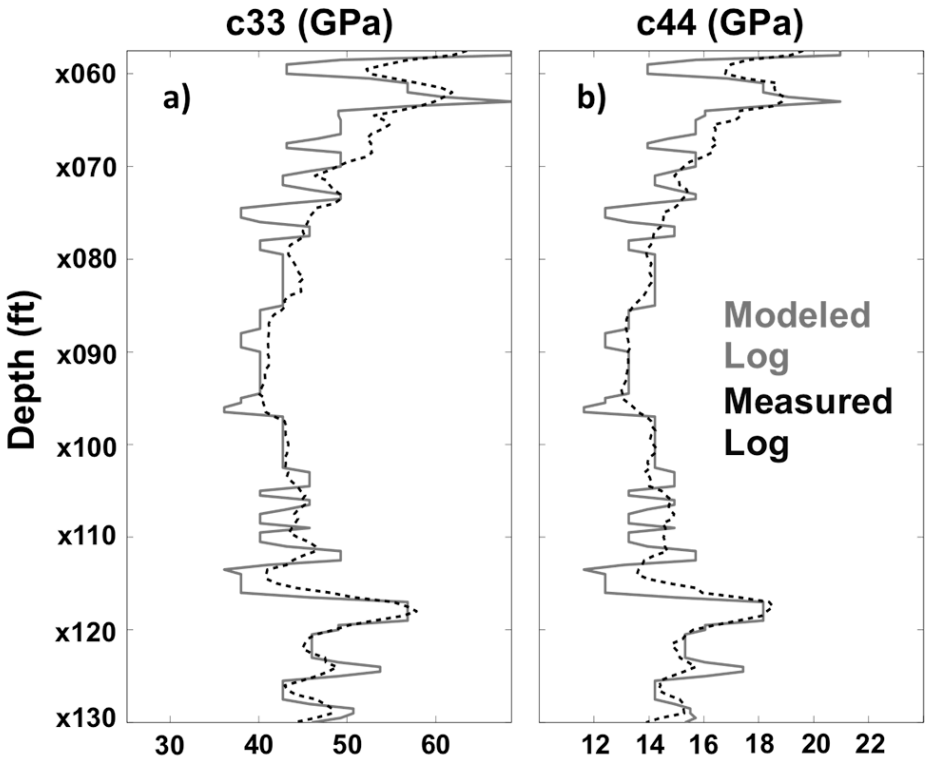

Figure 3.6: Modeled stiffness log for (a) c_{33}, and (b) c_{44}. In both figures, the red lines represent the modeled stiffnesses obtained by grid searching in the model space, and the black dashed lines represent the stiffnesses calculated form log measurements. As shown in this figure, the modeled stiffnesses agree with the measured stiffnesses fairly well.

In Figure 3.7, we evaluate the same dataset in Figure 3.5 in a different domain, by which the correlation between the clay volume and elastic properties become more evident. Figure 3.7 shows the crossplot of $(c_{33} - 2c_{44})\rho$ as a function of $c_{44}\rho$. The lines represent models of different clay volumes, and the points are the log measurements colored by clay volume. The measurements, from upper right to lower left, show the increasing clay volume trend. The models with clay volume increasing from 1% to 21% show the same trends as the measurements. Each model line covers a range of porosity plus kerogen volume from 0.04 to 0.16 from the top of each line to the bottom. However, at relatively large clay volume, the measured porosity plus kerogen volume is limited to a narrow range around 14%. These measured points are those points in orange at the bottom right in Figure 3.5. As a result, the 21% clay volume model line only crosses the measurements at its lowermost part.

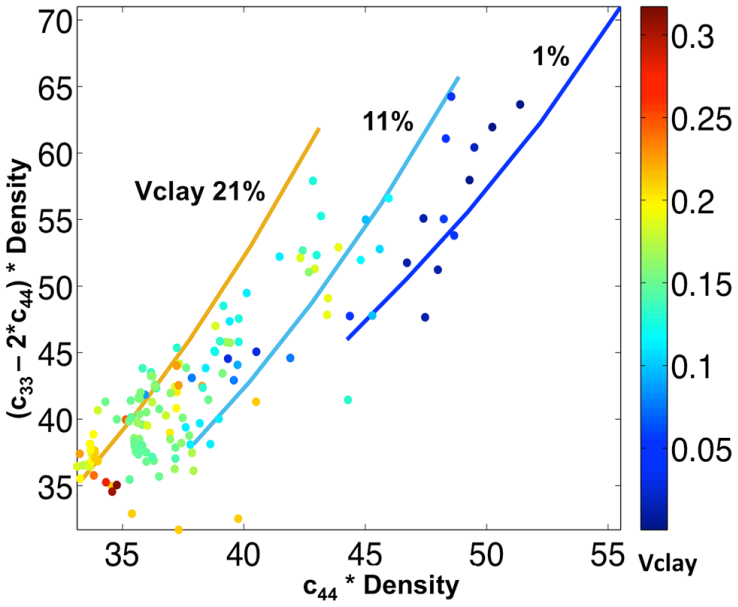

Figure 3.7: Crossplot of $(c_{33} - 2c_{44})\rho$ and $c_{44}\rho$. The lines are the models. The scattered points are calculated from log measurements, in color of clay volume. From upper right to lower left, both the measured points and models show the trend of increasing clay volume. Each model line covers a range of porosity plus kerogen volume from 4% to 16% from the top of each line to the bottom.

Based on the modeled stiffnesses, the Thomsen (1986) parameters were calculated, and their contour maps are shown in Figure 3.8. The modeled anisotropy increases with porosity plus kerogen volume. The increase of clay volume increases anisotropy at low clay concentration up to a turning point. The turning point corresponds to the clay volume, above which, the anisotropy is nearly constant, or slightly decreases, as clay volume continues to increase. We calculated the turning point for every modeled porosity plus kerogen value. This turning point is different for different values of porosity plus kerogen. The black lines connect these turning points in Figure 3.8. Superimposed on the color are the log measurements of clay volume as a function of porosity plus kerogen volume in Figure 3.8a and 8b (blue points). Most of the points fall in the epsilon range 0.17 to 0.3, and gamma range 0.17 to 0.27. This matches with values of 0.2 for epsilon and 0.18 for gamma obtained from laboratory-based directional velocity measurement. Pressure-dependent c_{13} measurements were not available, without which, the stiffness component c_{13} could not be pressure corrected. Therefore, the modeled Thomsen delta is not accurate. We compared the modeled anisotropy to the anisotropy parameters computed from Sone and Zoback (2013). The average composition for their samples included 15% clay, 10% kerogen, and 6% porosity, measured epsilon was 0.24, and measured gamma was 0.20.

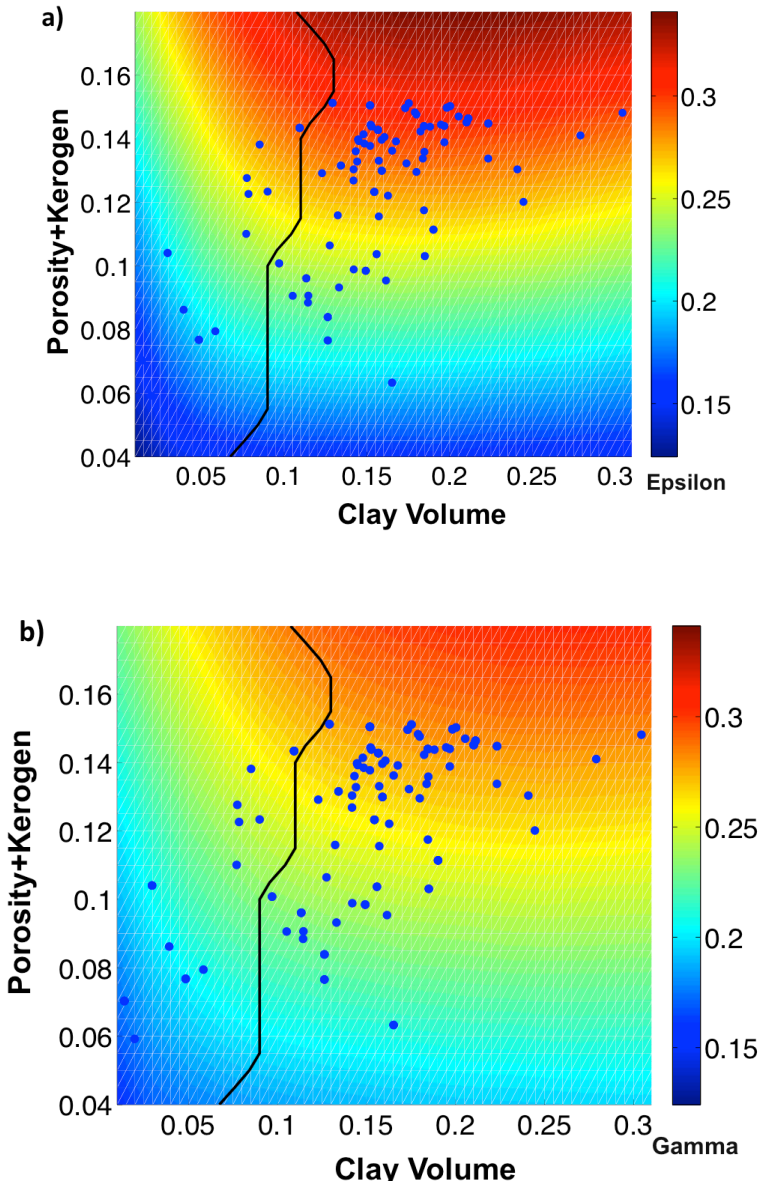

Figure 3.8: Contour map of (a) epsilon, and (b) gamma in space of {porosity plus kerogen volume} – Clay Volume. The scattered points are porosity plus kerogen volume versus clay volume, but they do not have an associated measured or calculated anisotropy value. The black lines in both pictures connect the turning points at every porosity plus kerogen volume.

Figure 3.9 demonstrates different correlations between anisotropy and clay volume. Using the same searching method to determine the stiffness logs, we built the anisotropy parameter pseudo logs (Figure 3.9a). In this figure, epsilon is in blue, and gamma is in red. The Thomsen parameters are relatively constant in the middle depth range, at about 0.3 for epsilon and 0.27 for gamma. At the top and base of the reservoir, the Thomsen parameters fluctuate. In Figure 3.9a, we compare the pseudo anisotropy logs to the clay volume. The black dashed lines are at depths corresponding to relatively low clay volumes, whereas the orange dashed lines correspond to depth with relatively high clay volumes. Figure 3.9b shows the crossplot of the gamma pseudo log and epsilon pseudo log for depth points whose corresponding clay volumes are to the left of turning points. This crossplot refers to the black dashed lines in Figure 3.9a. In Figure 3.9b, the depth points are colored by clay volume. Figure 3.9c is the same crossplot of gamma pseudo log and epsilon pseudo log for depth points whose corresponding clay volumes fall to the right of turning points. This crossplot corresponds to the orange dashed lines in Figure 3.9a. In Figure 3.9c, the depth points are colored by clay volume as well, but this time, the anisotropy, particularly epsilon, does not correlate with clay volume. Figure 3.9 reveals that at relatively low clay concentration, the anisotropy increases with clay volume, but at relatively high clay concentration, clay does not contribute to anisotropy.

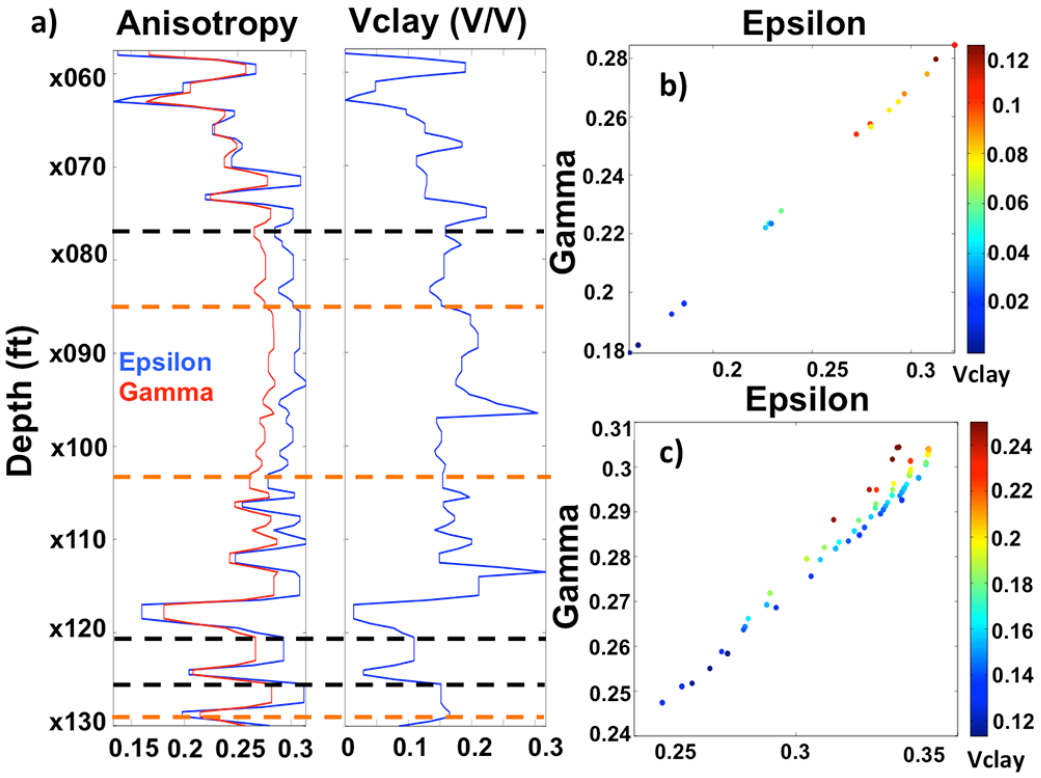

Figure 3.9: a) The anisotropy parameter pseudo logs, left (ε in blue and γ in red), and the clay volume on right. Black dashed lines indicate some depths where the anisotropy correlates with clay volume changing. Orange dashed lines indicate where the anisotropy does not correlate with clay volume. b) The crossplot of modeled ε and γ for the Upper Eagle Ford Shale. The points are the depth points where the clay volume falls to the left of the turning points, colored by clay volume. c) The crossplot of ε and γ. The points are the depth points where clay volume falls to the right of the turning points, colored by clay volume.

Johnston and Christensen's (1995) study on Devonian-Mississippian black shale formations showed that with a higher degree of clay alignment parallel to the bedding direction, the higher the degree of anisotropy for both P- and S- waves. The clay orientations in their study were detected by X-ray diffraction technology, and the anisotropy was calculated from laboratory velocity measurements. Similar to the Johnston and Christensen study, Allan et. al (2014) showed that the degree of alignment of clay matrix governed the effective anisotropy of organic-rich shale. The alignment degree of clay was more influential than volume of clay. They drew these conclusions based on both rock-physics laboratory measurements of ultrasonic velocity and high-resolution imaging techniques. From these previous studies on organic-rich shale, it is reasonable to suggest that the clay-anisotropy relation shown in Figure 3.9 is related to the preferred orientation pattern of clay clusters. Sone (2012) studied the clay mineral alignment of shale gas reservoir rocks of various shale formations using the scanning electron microscope. Figure 3.1 is one of these microscope images. He observed that at the local scale, the aggregates of aligned clay minerals were observed in all samples. These local scale clay mineral aggregates form many clay clusters. However, the preferred orientation of the clay clusters was not observed at core scale in many samples using optical microscopy. Combining the work of Johnston and Christensen, Allan et. al, and Sone, we suggested that the preferred orientation of clay clusters is preserved at low clay concentrations but vanishes at high clay concentrations for the Upper Eagle Ford Shale. Therefore, at relatively low clay concentration, the anisotropy increases with clay volume, but at relatively high clay concentration, clay does not contribute to anisotropy. One source of uncertainty of this anisotropic modeling is that we assumed the clay aspect ratios were constant when the clay concentration changes. However, the clay aspect ratio could change with concentration, and then could influence the modeled anisotropy.

3.5 DISCUSSIONS AND CONCLUSIONS

The micro-scale fabric strongly influences the elastic properties of the Upper Eagle Ford Shale. In shale, the complex composition, the platy clay minerals, non-spherical kerogen, and their preferred orientation patterns largely increase the complexity of the micro-scale fabric. Such a complex fabric affects the rock stiffness and induces effective anisotropy; therefore, it should be accounted for in the rock-physics modeling. In this paper, we presented a three-step rock-physics method to model the anisotropic elastic properties of the Upper Eagle Ford Shale. We started with the anisotropic DEM to construct a VTI effective medium, then we applied the orientation correction to compensate for the overestimated anisotropy caused by the fully aligned inclusions; finally, we applied the pressure adjustment to account for the different pressure-dependent behavior between P- and S-waves. The method accounted for the micro-scale fabric in terms of complex composition, shape and alignment of clay mineral, pore space, and kerogen.

The modeling results match the log measurements relatively well. Both the modeling results and log measurements show that the stiffness decreases with clay volume, kerogen volume and porosity. The correlation between elastic properties and clay volume, as revealed in this work, could be used to identify the regions with different clay concentration. The porosity and kerogen volume increase anisotropy, but the influence of clay volume on anisotropy is more complex. The anisotropy increases with clay volume at low clay concentration (Vclay < 10%); however, the anisotropy is nearly constant, or even lightly decreases, as clay content continuous to increase. This result suggests that a preferred orientation of clay clusters is preserved at low clay concentration but vanishes at high clay concentration in the Upper Eagle Ford shale. In addition, using this method we are able to map the rock properties to anisotropy

parameters and build the anisotropy parameter pseudo logs. The estimation of the anisotropy is another potential application of this three-step rock-physics method.

Uncertainty of the rock physics modeling comes from multiple aspects. Firstly, the petrophysical inversion for rock composition is non-unique. Rock composition is one of the most influential factors for rock physics modeling. Secondly, various studies showed that aspect ratios are highly influential on the DEM model. There is no direct measurement available to identify mineral and pore space aspect ratios; the inclusion aspect ratio values of each mineral and pore space applied in this chapter were based on multiple numerical experiments. Thirdly, I used the compaction model to simulate the orientation distribution function of clay clusters. The compaction factor in the compaction model was also set based on multiple numerical experiments. Fourthly, I modified Sone and Zoback's (2013) pressure-dependent directional stiffness measurements for the Eagle Ford Shale from another location for pressure adjustment of Eagle Ford Shale in the study area of this chapter. The reference effective pressure was set based on multiple tests as well. Both the measurements and the reference effective pressure contribute uncertainty to the modeled stiffnesses. For these four types of uncertainty, there are no explicit equations to calculate how large the uncertainty is. However, sensitivity analysis of the influence of each factor on modeled stiffnesses could provide an estimate of the uncertainty.

This method could also be applied to other shales with carefully chosen parameters. The appropriate inclusion aspect ratios, ODFs, and pressure-dependent compressional and shear stiffnesses ratio need to be determined. In the Upper Eagle Ford Shale case, we investigate how clay volume, kerogen volume, and porosity influence the stiffnesses and anisotropy. However, this method is not limited to clay, kerogen, and

porosity. We could model and interpret the anisotropic stiffnesses with respect to other influential parameters based on careful investigation for each particular shale formation.

Chapter 4: Geostatistics Guided Seismic Inversion of 3D Seismic Data From Eagle Ford Shale

4.1 ABSTRACT

Thin-bed effects and anisotropy are two important factors limiting the use of conventional seismic characterization of Eagle Ford shale. To circumvent these issues, I use the geostatistics guided GAIS inversion. The geostatistical models simulate small-scale vertical variations that are below seismic resolution; the geostatical realizations of the well logs are used as a priori models and the GAIS inversion quickly searches for the most probable pseudo-logs at all surface locations. GAIS uses the greedy importance sampling method based on multiple parallel very fast simulated annealing results. It explicitly explores the target distribution by grid search of the important regions with fixed step lengths along axis-parallel directions. This method performs an optimal balance between computational efficiency and accuracy of estimation. As to anisotropy, I used Ruger's VTI model to account for anisotropy in forward modeling. This geostatistics guided inversion was applied on a pre-stack 3D seismic data to estimate the reservoir elastic properties and anisotropy parameters of Eagle Ford shale. In our results, the Lower Eagle Ford is clearly resolved in the inverted impedance volume. The sharp boundary and large impedance contrast between Eagle Ford and Buda are also very clear in GAIS inverted impedances. In addition, because of the accounted anisotropy, the quality of inverted S-impedance is significantly improved. The thin-bed issue and

anisotropy are common issues in seismic reservoir characterization. The methods I applied on Eagle Ford shale can also be applied to data from other reservoirs.

4.2 INTRODUCTION

The Eagle Ford shale is the upper Cretaceous shale located in south Texas. It is overlain by the Austin Chalk and underlain by the Buda Limestone (Hentz and Ruppel, 2010). Eagle Ford contains two sub-formations: Upper Eagle Ford and the Lower Eagle Ford. Although both Upper and Lower Eagle Ford are hydrocarbon reservoirs, the Lower Eagle Ford has higher organic content and higher porosity. However, our study is focused in an area in which the Lower Eagle Ford is a thin layer with thickness varying from 0 to 40ft. This thin layer is not resolvable using conventional seismic data analysis. One objective of this paper is to resolve both Upper and Lower Eagle Ford Formations in the inverted impedance volume. This thin-bed issue is a common problem in seismic characterization. Because of its band-limited nature, seismic data cannot resolve thin layers below one-eighth of a wavelength in thickness (Widess, 1973). However, such thin layers might be significant reservoirs or sweet spots inside reservoirs, especially in unconventional reservoirs. The method used in this paper could be applied to solve thin-bed issues for other reservoirs as well.

The other issue that is addressed in this paper is anisotropy. Anisotropy influences seismic waves by affecting their amplitude, travel time and ray paths; further, it introduces and propagates errors in inversion and amplitude versus offset analysis that assume isotropy (Sayers, 2005). In addition, works by Crampin (1981, 1985), Lynn and Thomsen (1986), and others demonstrated that anisotropy has first order influence on shear and mode-converted PS-waves. Seismic velocity measurements in the laboratory indicate that shale exhibits VTI symmetry, with the symmetry axis perpendicular to

bedding direction (e,g., Vernik and Nur, 1992, Jones and Wang, 1981, and Wang, 2002). The laboratory-measured anisotropy for Eagle Ford Shale in our study area are 0.15 for ϵ and 0.07 for δ. Exact equations for plane wave reflection coefficients are very complex even for isotropic media. Therefore, most reflection coefficients are calculated based on different level of approximation. Barnik (1987) used the Thomsen parameter δ, the difference between the P-wave and SV- wave anisotropies of the medium, to describe the effects of transverse isotropy on P-wave reflection amplitude. He expressed the reflection coefficient in linearized terms of changes in elastic properties. By this approximation, the observed systematic depth errors in the North Sea were corrected. However, this approximation only works for small propagation angles. Ruger (1997) used both ε and δ to describe the anisotropy effect on transverse isotropic medium. ε represents the P-wave anisotropy. His approximation is valid for propagation angle range up to 40 degrees. Both Barnik's (1987) and Ruger's 1997 expression of P-wave reflectivity are based on weak-contrast, weak-anisotropy assumptions. For the measured anisotropy of Eagle Ford, Ruger's expression is still valid, and I used this approximation for forward modeling. The results showed that the quality of inverted S-impedance by anisotropic inversion is significantly improved, compared to the isotropic inversion.

For the thin-bed issue, many different inversion methods have been developed to improve the impedance resolution. Sparse seismic inversion methods (e.g. Reil and Berkhout, 1985) have been reported in which reflectivity solutions contain frequency beyond the original seismic data. Zhang and Castagna (2011) developed the basic pursue inversion (BPI) method to construct the reflectivity series from post-stack seismic reflection data. This method uses basis pursuit decomposition (Chen et al., 2001) to decompose the seismic trace to a wavelet dictionary, which consists of even and odd thin layer seismic response. Then seismic traces are constituted as a superposition of these

seismic response patterns. Based on wedge model tests, Zhang and Castagna (2011) suggested that BPI could better resolve thin beds than comparable sparse-spike inversion. The downside of BPI is that it depends on the correct wavelet. A sparse layer inversion similar to BPI implemented in frequency domain is spectral inversion (Partyka, 2005; Portniaguine and Castagna, 2004, 2005; Puryear and Castagna, 2006, 2008). Marfurt and Kirlin (2001) showed the effectiveness of seismic spectral decomposition as a thickness-estimation tool. Spectral inversion (Partyka, 2005; Portniaguine and Castagna, 2004, 2005; Puryear and Castagna, 2006, 2008) uses spectral decomposition to unravel the thin-bed reflectivity created complex interference patterns, and then uses these patterns to invert for the original reflectivity. Based on spectral shape information, spectral inversion provides better vertical resolution and improves the thickness estimation.

In this chapter, I propose to use geostatistic guided stochastic seismic inversion for Eagle Ford Shale to resolve the thin-beds. Geostatistical models are built based on well logs using the kriging technique (Haas and Viallix, 1976; Xu, et. al 1992; et. al). Kriging (Krige, 1951, Matheron, 1970) is the first applicable geostatistical method. It is essentially a generized linear algorithm that extends the data-to-data correlation to data-to-unknown relation. Based on the basic system, there are different modifications to adapt various situations, for example, ordinary kriging (Goldberger, 1962), cokriging (Goovaerts, 1997) etc. Extending the kriging idea beyond two-point simulation, there are covariance-based simulation algorithms, like sequential Gaussian simulation (Deutsch and Journel, 1998). Kriging based techniques (including sequential Gaussian simulation) still remain a major data integration tool, which is widely used in most geostatistical estimation and simulation algorithm.

Compared with seismic data, the geostatistical models include small-scale vertical variations that are not revealed by seismic data because of its band-limited nature. Using

a geoststistical model as an initial model compensates the seismic data for small scale variation (Bosch, 2010). This feature is especially beneficial for thin-beds, since they cannot be resolved using conventional seismic data analysis, but are clearly identified in geostatistical models. Also, geoststistical models are constrained by spatial correlation; therefore, the models are geologically consistent. The downside of geostatistical models is that they are inadequate for lateral heterogeneity (Hass and Dubrule, 1994). The inversion process modifies and validates the initial geostatistical model with seismic data.

I chose greedy annealing importance sampling (GAIS) (Xue et.al., 2011; Xue, 2013) method as the inversion algorithm. GAIS is a stochastic process that combines very fast simulated annealing (VFSA) (Ingber, 1989) and greedy importance sampling (GIS) (Schuurmans and Southey, 2000, 2002). Compared to the Markov Chain Monte Carlo (MCMC) based important sampling methods, VFSA provides fast convergence to the highest peak of the posterior probability function by reducing the random walk behavior. It is an efficient method, but the results might be biased when the distribution of samples is skewed (Sen and Stoffa, 2013). Compared to VFSA, GIS provides unbiased estimation independent of the prior distribution and improves inferences quality. However, GIS requires each individual searching block must contain at least one or two important points. Also, although GIS is independent of a prior probability distribution, the locations of the starting points for use in greedy search are essential for fast convergence and accurate estimation, especially in a high dimensional problem. For those two reasons, it is important to start GIS with proper starting points in prior distribution. Xue (2011, 2013) modified the GIS to the new GAIS methods in order to optimize the balance between computational efficiency and accuracy of estimation. Instead of sampling directly from prior distribution, GAIS applies multiple VFSA threads first and uses the end points of

each VFSA thread as an initial point for greedy search. Since VFSA can converge to some important region GAIS speeds up GIS.

In this chapter, I first describe the algorithm of GAIS in brief, and the details of implementation of the algorithm. Then I show the GAIS seismic inversion on Eagle Ford using the geostatistical initial model. The geostatistical initial model was built by sequential Gaussian simulation. The inversion model parameters include P-, S-impedance, δ, and ϵ at each time sample. The inverted P- and S- impedances are compared with inversion results using those from conventional deterministic methods.

4.3 METHODOLOGY

In this section, I explain how to implement the GAIS algorithm. In additional to the inversion algorithm, seismic inversion involves forward modeling, defining the objective function (error function), and setting up an initial model. The methodologies used in these four parts will also be explained in this section.

Figure 4.1 shows the algorithm of GAIS. Multiple independent VFSA threads are applied first; then each result from VFSA thread is expanded to a block of points. The local minimum of the objective function in each expanded block is found in step 3 as the final samples, and the corresponding weight to those final samples are assigned in step 4. The local minimum of the objective function in an expanded block corresponds to the local maximum of the likelihood function, which is $\mathrm{P}(d|\mathrm{m}) \sim Q(m) * \mathrm{e}^{-|\mathrm{E}|}$. $\mathrm{P}(d|\mathrm{m})$ is the conditional probability, Q represents the prior distribution, and E is the objective function. Because the prior distribution is a uniform distribution, the likelihood function reduces to $\mathrm{P}(d|\mathrm{m}) \sim \mathrm{e}^{-|\mathrm{E}|}$. Finally, the weighted average of the final samples are calculated as the expectation of true model. The detailed algorithm for VFSA is shown in Figure 4.2. The next issue is how to define the weighting function

$w_i(m_j) = P(m_j)\alpha_{i,j}/Q(m_i)$ in step4. Here P represents the distribution of true model. The prior distribution Q is constructed from VFSA. Although the exact shape of distribution of true model P is unknown, it is known that $P(m) \propto e^{-|E|}Q(m)$ for a Gibbs distribution at temperature equals one; where E is the objective function. Therefore, I will have $w_i(m_j) \propto e^{-|E|}$.

Step 1: Apply multiple independent VFSA threads, whose results provide the model set **m**.

Step 2: Fro each m_i belongs to **m**, let $m_{i,1} = m_i$. Compute block $B_i = \{m_{i,1}, m_{i,2}, \ldots m_{i,n}\}$ by taking local steps in the direction of minimum $E(m)$ (equals to maximum $|f(m)P(m)|$) until reached a local minimum or n-1 steps.

Step 3: Create the final sample from the blocks of points

$m_{1,1} \ldots m_{1,n}, m_{2,1} \ldots m_{2,n}, \ldots, m_{q,1} \ldots m_{q,n}$.

Step 4: Assign each point m_j belongs to block B_i with a weight

$$w_i(w_j) = P(m_j) a_{i,j} / Q(m_i)$$

Where m_i is the initial point from block B_i, m_j is one of the successors in its block and α_{ij} is relative arbitrary beside the must satisfy $\sum_{m_i \in M} \alpha_{i,j} I_{i,j} = 1$

Step 5: Estimate the expectation value of model m by weighted summary of all the samples together.

$$E_m = \frac{1}{n} \sum_{i=1}^{n} \sum_{j=1}^{k} m_{ij} w_i(m_j)$$

Figure 4.1: Algorithm for Greedy Annealing Importance Sampling (GAIS) (Xue et al, 2013).

start at a random location with $\mathbf{m}_0$ with energy $E(\mathbf{m}_0)$

loop over temperature (T)

- loop over number of random moves/temperature
- - loop over model parameters i=1, … , NM
- - - $u_i \in U[0,1]$
- - - $y_i = \mathrm{sgn}\left(u_i - \frac{1}{2}\right) T_i^{mod}\left[\left(1+T_i^{mod}\right)^{|2u_i-1|} - 1\right]$
- - - $m_i^{new} = m_i^{old} + y^i\left(m_i^{max} - m_i^{min}\right)$
- - - $m_i^{min} \le m_i^{new} \le m_i^{max}$
- - end loop
- - now we have a new model $\mathbf{m}^{new}$
- - $\Delta E = E(\mathbf{m}^{new}) - E(\mathbf{m}_0)$
- - $P = \exp\left(-\frac{\Delta E}{T}\right)$
- - if $\Delta E \le 0$, then
- - - $\mathbf{m}^0 = \mathbf{m}^{new}$
- - - $E(\mathbf{m}^0) = E(\mathbf{m}^{new})$
- - end if
- - if $\Delta E > 0$, then
- - - draw a random number $r = U[0, 1]$
- - - if $P>r$, then
- - - - $\mathbf{m}^0 = \mathbf{m}^{new}$
- - - - $E(\mathbf{m}^0) = E(\mathbf{m}^{new})$
- - - endif
- - endif
- end loop

end loop

Figure 4.2. A pseudo FORTRAN code of VFSA (Sen and Stoffa, 2013).

The objective function used here is normalized L2 norm of the difference between the synthetic seismogram and observed seismic data as follows (Srivastava and Sen, 2010):

$$\mathrm{obj} = \frac{2\sum_{i,j}(S_{obs} - S_{syn})^2}{\left(\sum_{i,j}(S_{obs} + S_{syn})^2 + \sum_{i,j}(S_{obs} - S_{syn})^2\right)}, \tag{4.1}$$

where S_{obs} represents the amplitude of observed seismogram, and S_{syn} represents the amplitude of synthetic seismogram generated by forward modeling. Note that this objective function is similar to the L2 norm of data misfit. The forward modeling algorithm contains two parts: generating reflectivity series R at each boundary of time samples, and generation of a synthetic seismogram from the reflectivity series. In this paper I used Ruger's transversely isotropic model (Ruger, 1997) to generate the reflectivity series, and applied the convolution model (Cooke and Schneider, 1983) for seismogram generation. The assumption of modeling the Eagle Ford Shale using Ruger's VTI model increases the uncertainty of the forward modeling. This uncertainty could be accounted for in an updated objective function as

$$obj(m) = 1/2\left(S_{obs} - S_{syn}\right)^T C_D^{-1}\left(d_{obs} - S_{syn}\right), \tag{4.2}$$

where S_{obs} is the measured seismogram, S_{syn} is the synthetic seismogram, and C_D is the data covariance matrix, which contains both observation error and theory (modeling assumption) error.

The convolutional model (Cooke and Schneider, 1983) is a typical forward modeling algorithm for model-based inversion. At normal incidence, a seismic trace can be calculated by $S = W * R + N$ (4.3) Here S is the synthetic seismic data trace; W represents the wavelet extracted from the seismic and well log data, or a synthetic wavelet; R is the reflectivity series, and N is the random noise.

R is calculated by Ruger's anisotropic model (Ruger, 1997) for vertical transverse isotropic (VTI) medium. The P-P wave reflectivity coefficient at the boundary of an isotropic layer over a VTI layer is calculated as:

$$R_{pp}(\theta) = \frac{1}{2}\frac{\Delta Z}{\bar{Z}} + \frac{1}{2}\left\{\frac{\Delta V_{p0}}{\bar{V}_{p0}} - \left(\frac{2\Delta V_{s0}}{\bar{V}_{s0}}\right)^2 \frac{\Delta G}{\bar{G}} + \Delta\delta\right\}\sin^2\theta + \frac{1}{2}\left\{\frac{\Delta V_{p0}}{\bar{V}_{p0}} + \Delta\epsilon\right\}\sin^2\theta\tan^2\theta, \quad (4.3)$$

where θ represents the wave propagation angle, $Z = \rho V_{p0}$ is the vertical P-wave impedence, $G = \rho V_{s0}^2$ represents the vertical shear modulus, δ and ϵ represent Thompson parameters. The prefix Δ indicates the difference between upper and lower layer, and $\bar{}$ represents the average of two layers. Convolving the reflectivity coefficient series with the wavelet using Equation 6 provides the synthetic seismogram.

I used Sequential Gaussian Simulation (SGS) (Deutsch and Journel, 1998) to generate the geostatistical initial model. SGS is commonly used for continuous variables simulation, and it is used to generate the P- and S-impedances in this paper. There are four basic steps in SGS: 1) generate a random path through the given simulation grid; 2) visit the first node along the path and use kriging to estimate a mean and standard deviation for the variable at that node based on surrounding data values; 3) randomly select a value from the corresponding normal distribution generated in previous step, and set the selected value to this node; 4) visit the successive nodes in the random path and repeat step 1-3 until all nodes in the random path has been assigned a value.

Kriging applied in step 2 estimates the value of random node from the surrounding nodes using Equation 4.4. In Equation 4.4, $Z^*(u)$ stands for the value at the random node, $Z(u_\alpha)$ stands for the value of surrounding nodes, m is the mean value, and λ_α is the weight for corresponding surrounding node that minimize $E\{Z(u) - Z^*(u)\}$. The variance of $Z^*(u)$ is $\sigma^2 = Var\{Z(u) - Z^*(u)\}$.

$$Z^*(u) - m = \sum_\alpha \lambda_\alpha [Z(u_\alpha) - m]. \quad (4.4)$$

In this chapter, I used the geostatistical model built by SGS as the initial model for GAIS inversion, the Ruger's transverse isotropic model and convolutional model to implement the forward modeling, and GAIS as inversion algorithm to invert the P-, and S- impedance and anisotropy of Eagle Ford shale from pre-stack 3D seismic data.

4.4 DATA

The study area is located in Maverick Basin in south Texas; the project includes pre-stack seismic data and two wells.

4.4.1 Seismic Data

The 3D seismic data is shown in Figures 2.6 and 2.8: stacked P-P seismic data (Figure 2.6) and pre-stack P-P gathers (Figure 2.8). Each trace contains 2001 samples with a sampling interval of 2ms, and the space between traces is 82.5ft. The pre-stack gathers were transformed to angle gathers using the velocity model provided by Shell Oil Company. The offset range is 4 – 42 degree, and I used 4 – 34 degree range for GAIS inversion. The tow horizons in Figure 2.6 and 2.8 are Eagle Ford and Buda; the interface between the Upper and Lower Eagle Ford cannot be resolved from seismic data. I used angle – dependent statistical wavelets extracted from angle gathers for inversion. The wavelets are shown in Figure 2.9.

4.4.2 Well Data

I have measurements from two wells (Well B4 and B7 shown in Figure 2.10 and Figure 2.11), including gamma ray, density, P-wave, and S-wave velocities. P-wave and S-wave velocities are highly correlated, but independently measured. The thick red lines in Figure 2.10 and 2.11 indicate the top and base of the Eagle Ford Shale. The Eagle Ford

Shale is clearly separated from Austin Chalk and Buda Limestone in Density, Vp, and Vs. Gamma ray (GR) shows gradually increasing from Austin Chalk to Eagle Ford, and sharply decrease towards Buda Limestone. In well B4 (Figure 2.10), from 8650 – 8700ft, there is a significant thin layer above Buda with high GR, low density, and low velocity. This thin layer is the Lower Eagle Ford. In well B4, the Lower Eagle Ford thickness is about 35ft, however, the Lower Eagle Ford is negligible in well B7.

4.5 RESULTS

I applied trace-by-trace GAIS inversion method on pre-stack seismic data to estimate the reservoir elastic properties and anisotropy parameters. The model parameters are P-, S- impedance, δ, and ϵ at each time sample. Forward modeling uses Ruger's anisotropic model (Ruger, 1997) to calculate the reflection coefficient series, and convolving the reflection coefficient series with wavelets to generate synthetic seismograms. The objective function used here is defined by Equation 5. The initial models of P- and S- impedance and density are built based on well logs using Stanford Geostatistical Modeling Software (SGeMS). The assumption for the initial models is that the variograms of impedances and density are the same in the horizontal direction and vertical direction. The variograms in the vertical direction are calculated from log measurements at the log scale. Besides wells B4 and B7, I also used other wells in the Eagle Ford Shale that are outside of the seismic area to construct our initial model. The initial models for anisotropy are set at: ϵ equals 0.15 and δ equals 0.07 for Eagle Ford; ϵ equals 0 and δ equals 0 for both Austin Chalk and Buda. These values are determined based on lab measurements provided by the sponsor. GAIS inversion control parameters include cooling schedule, number of parallel VFSA, number of iterations per VFSA, step length, the number of steps for greedy search. Based on multiple tests, I used 10 VFSA

threads with 200 iterations per VFSA, and 100 steps of greedy search after each VFSA. The step lengths for P- and S- impedance were set as 20, and were set as 0.01 for δ and ϵ. The cooling schedule is $T = T_0 e^{-ck^{1/D}}$, where I chose $T_0 = 10$, $D = 0.45$, and k is the iteration number.

Figure 4.3 shows the change of error function with iterations on a single trace. I compared the GAIS result with the deterministic inversion results using standard low frequency initial model. The deterministic inversion is done using a commercial software.

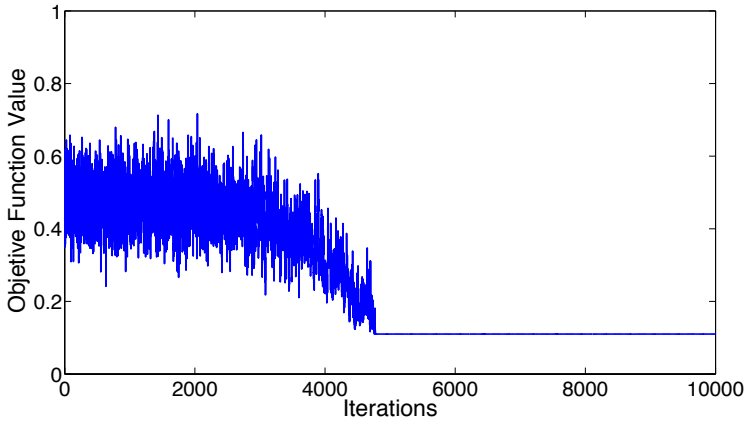

Figure 4.3. error function change with VFSA + GIS at well B4.

The inverted P- and S- impedances at the well locations are shown in Figure 4.4. The results from GAIS (blue lines) inversion match the well logs very well. The inverted impedances resolves the decreasing trend in Eagle Ford, the thin Lower Eagle Ford with low impedances in well B4, and the sharp boundaries between Eagle Ford and Buda. However, the deterministic inversion method (magenta lines) works like a low frequency filter for impedance logs. The inverted impedances miss the sharp boundaries between Eagle Ford and Buda at both wells, as well as the low impedance of the Lower Eagle Ford at well B4. At well locations, the GAIS inverted results are very close to the initial model as expected. But away from well location, the inverted impedances are different from those in the initial model; the differences are shown in Figure 4.6.

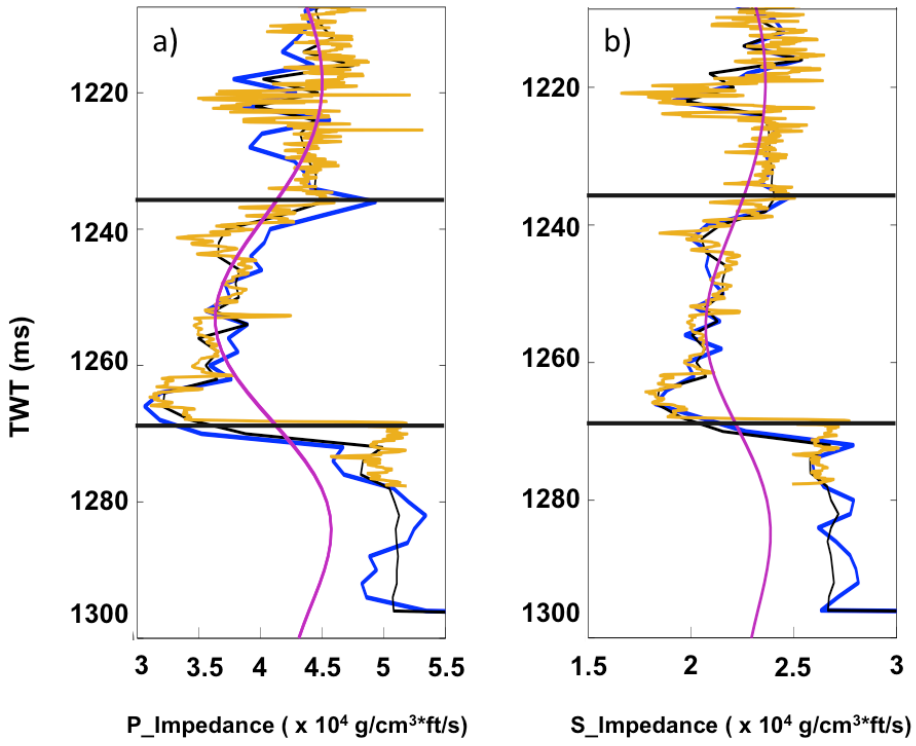

Figure 4.4 (caption next page)

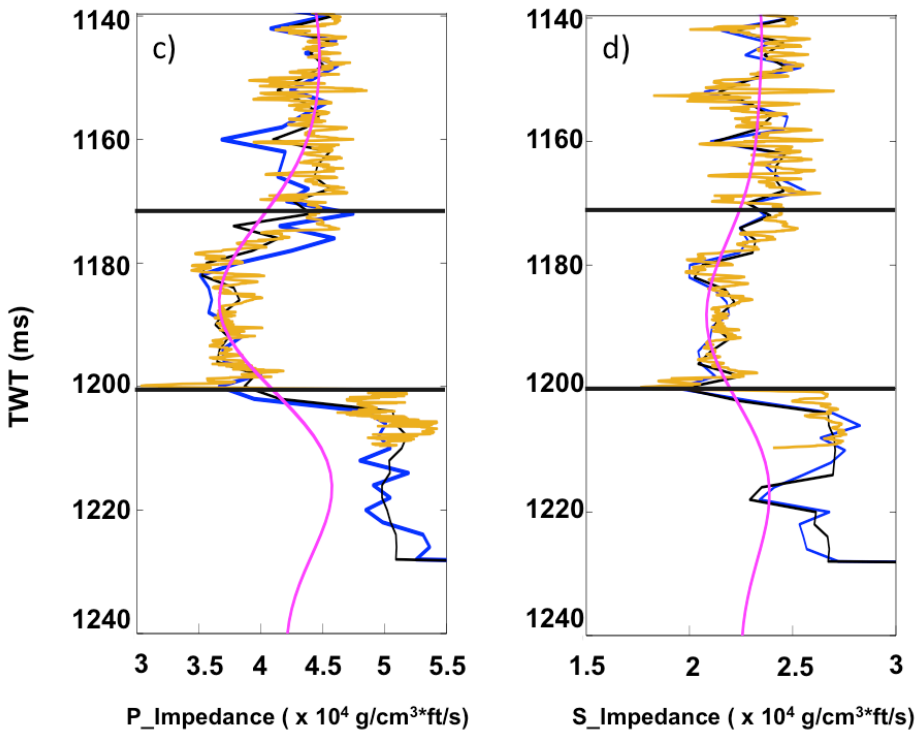

Figure 4.4. Comparing between GAIS inversion and deterministic inversion results at well B4 (a, b), and B7 (c, d). Left two figures (a, c) are P-impedance, and right two figures (b, d) are S-Impedance. In all four figures, the yellow color lines represent the measured logs, blue lines represent the GAIS inverted impedances, black lines represent the geostatistical initial model, and magenta lines represent the inverted impedances by deterministic method. Three black horizontal lines in each figure are tops of Austin Chalk, Eagle Ford, and Buda. The initial model used for deterministic method was standard low frequency model generated in Hampson Russell. Eagle Ford formation is the target reservoir.

Figure 4.5 shows the inverted P- and S- impedances on a 2D section. The updates of initial P- and S- impedance models from GAIS on the same 2D section are shown in Figure 4.6. GAIS inversion results (Figure 4.5a, c) show a decrease in impedance in Eagle Ford, and it varies laterally. The thin the Lower Eagle Ford with lower impedance is clearly identified in the inverted P- and S- impedance sections and the volume. The sharp boundary and large impedance contrast between Eagle Ford and Buda are very clear in the GAIS inverted impedances. Compared to them, in deterministic method inverted impedances plot (Figure 4.5b, d), Eagle Ford is a block with relatively lower impedance other than Austin Chalk and Buda. The boundary between Eagle Ford and both Austin Chalk and Buda are ambiguous in P-impedance (Figure 4.5b). The large S-impedance contrast between Eagle Ford and Buda is not clear in Figure 4.5d. In addition, the GAIS inverted impedances show higher lateral variation, but the continuity is still preserved. The inverted S-impedance is highly improved by GAIS method. One reason for this improvement is that I accounted for the anisotropy in GAIS inversion. Works by Crampin (1981, 1985), Lynn and Thomsen (1986), and others showed that anisotropy has first order influence on S-impedance. Also, as shown in Equation 7, both S-impedance and anisotropy influence the amplitude/reflectivity at mid-high angle range. Without accounting anisotropy independently, the anisotropy influence on amplitude will be superimposed to S-impedance.

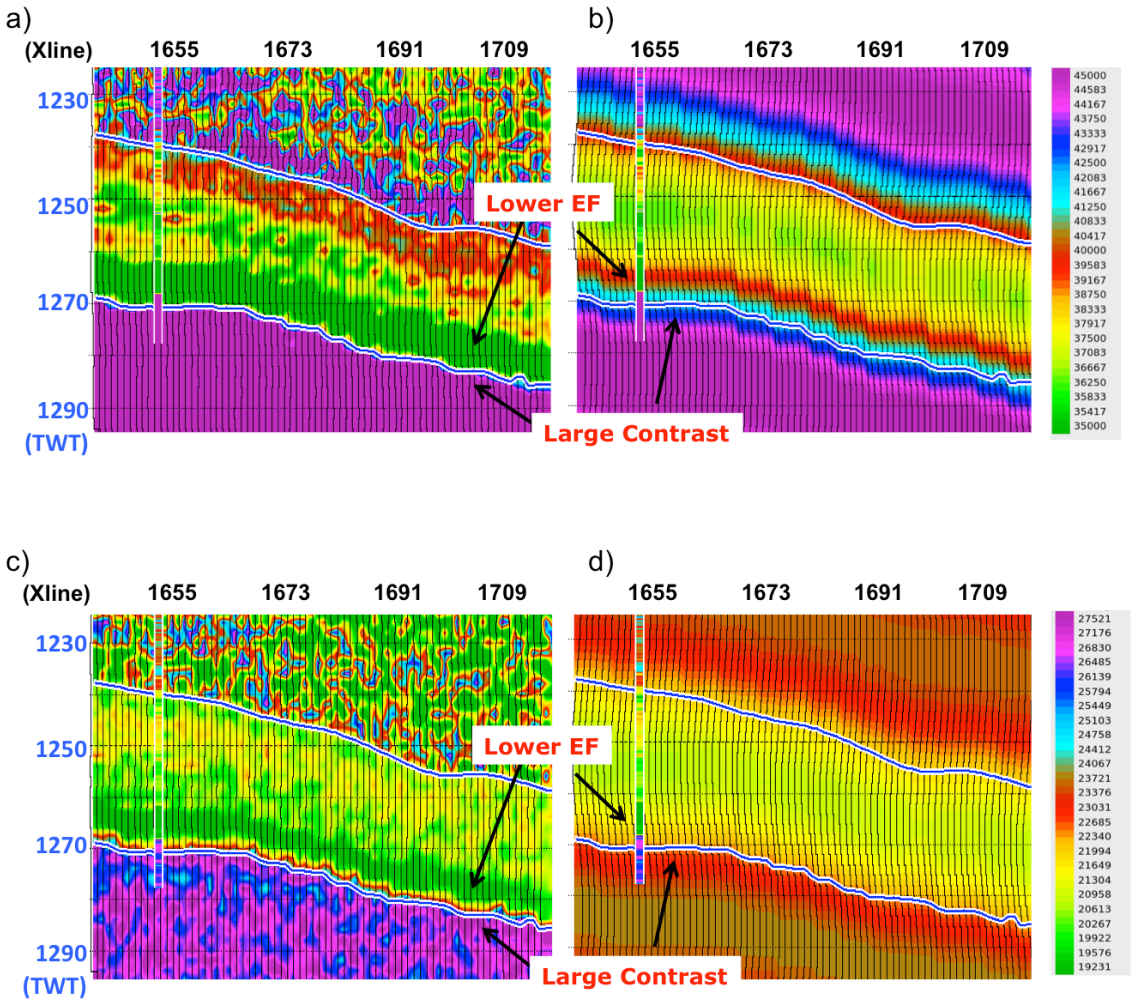

Figure 4.5. Comparison between GAIS inverted impedances (a, c) and deterministic method inverted impedances (b, d) at IL690 in two way travel time. Top two figures (a, b) shows inverted P-impedances, and bottom two figures (c, d) shows inverted S-impedances. The inserted well is well B4 in color of calculated impedances from measurements (P-impedance for (a, b); S-impedance for (c, d). In all four figures the horizontal blue lines, from top to bottom, represent horizon Eagle Ford and Buda. The inversion window of GAIS is from upper Austin Chalk to upper Buda. The magenta color above and at upper part of Austin Chalk in (a, c) are the area out of inversion window. Eagle Ford formation is the target reservoir.

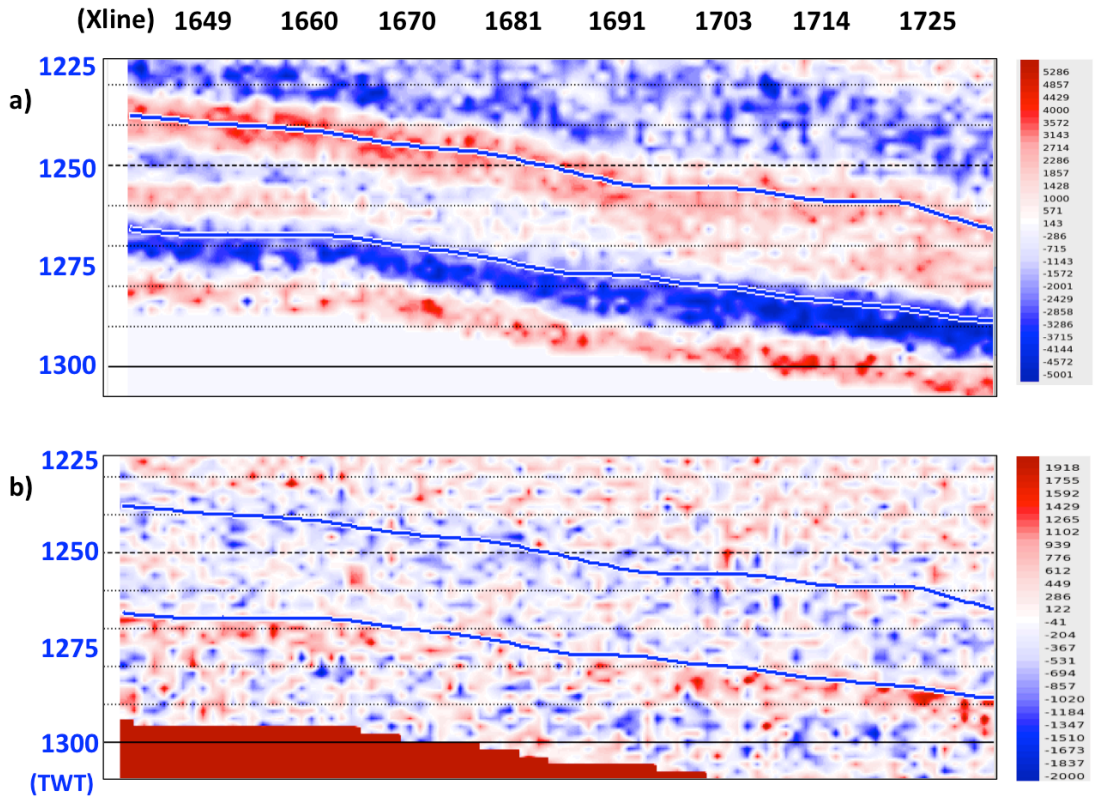

Figure 4.6. The difference between GAIS inverted impedances and the initial models at IL690 in two way travel time: (a) updates on P-impedance, and (b) updates on S-impedance. The white (a) and red (b) colored areas on top and bottom part of each figure are areas out of inversion window.

Figure 4.7 shows the inverted P- and S- impedances on a horizon slice (The middle horizon slice between Eagle Ford and Buda). Figures 4.7a and 4.7c are seismic amplitude date on the horizon slice; Figure 4.7b and Figure 4.7e are GAIS inverted P- and S- impedance; and Figure 4.7c and 4.7f are deterministic method inverted P- and S- impedance. Comparing inverted P-impedance with post-stack seismic amplitude (a – c), I observed that the GAIS inversion preserved the lateral variation and continuity better than the deterministic method. The northeast to southwest strip patterns of seismic amplitude is well reflected in the GAIS inverted P-impedance within the entire survey area. In Figure 4.7d – f, I compare the inverted S-impedance with the difference of pre-stack seismic amplitude between middle angle range and small angle range. As shown in Equation 7, the near angle reflectivity is determined by P-impedance only, and the S-impedance influences middle angle reflectivity. Therefore, the post-stack seismic amplitude is determined by P-impedance, while middle angle pre-stack seismic amplitude is influenced by both S-impedance and P-impedance. That is the reason why I compare inverted P-impedance with post-stack seismic data, but compare S-impedance with the difference between middle angle and near angle pre-stack seismic data. The amplitude variation from northeast to southwest in Figure 4.7d is reflected in S-impedance variation in Figure 4.7e, but not in Figure 4.7f. Figures 4.7e and 4.7f represent the inverted S-impedance using GAIS method and deterministic method respectively. Figure 4.7 shows that GAIS provides better inverted impedance in terms of lateral continuity and variation.

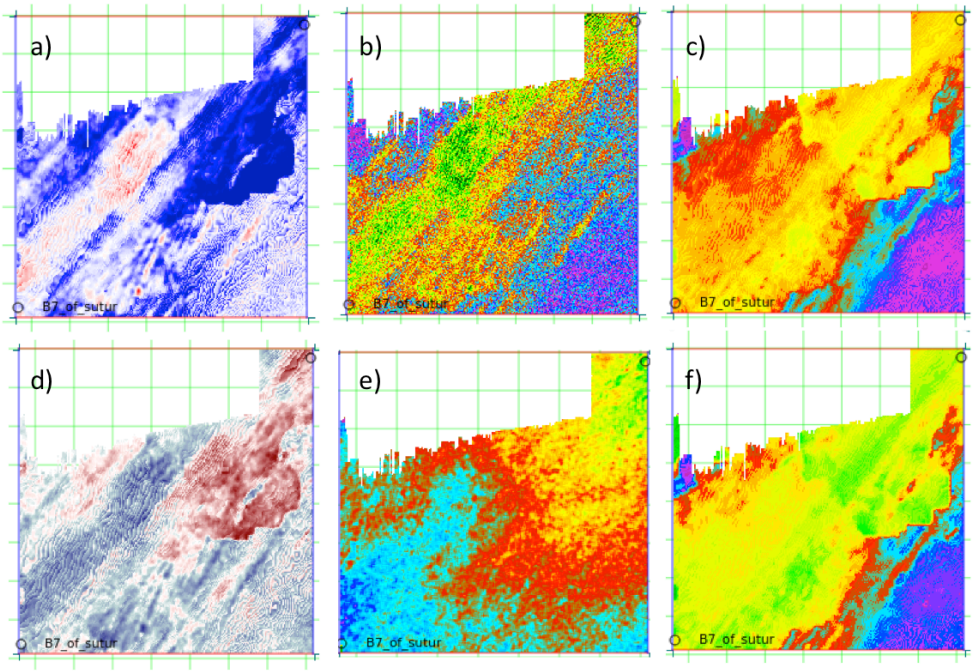

Figure 4.7. A horizon slice inside Eagle Ford colored with post-stack seismic amplitude (a), GAIS inverted P-impedance (b), deterministic method inverted P-impdance (c), difference of pre-stack seismic amplitude between middle angle range and small angle range (d), GAIS inverted S-impedance (e), and deterministic method inverted S-impdance (f). The P-impedance slices (b, c) have the same color bar, and the S- impedance slices (d, e) have the same color bar as well.

Besides P- and S- impedances, GAIS inversion also updates the Thompson parameters ϵ and δ. Figure 4.8 shows inverted ϵ (a), and δ (b). Austin Chalk and Buda are isotropic; therefore, ϵ and δ for these two formations are 0. The inverted ϵ is around 0.15, and inverted δ is around 0.07. The anisotropy in the Lower Eagle Ford is relatively higher than that in the Upper Eagle Ford, but the lateral variation is small. Compared with the initial model, GAIS inversion provides some lateral variation for anisotropy, but overall the updates are limited. Since I are using the lab-measured values as initial model, negligible update is expected.

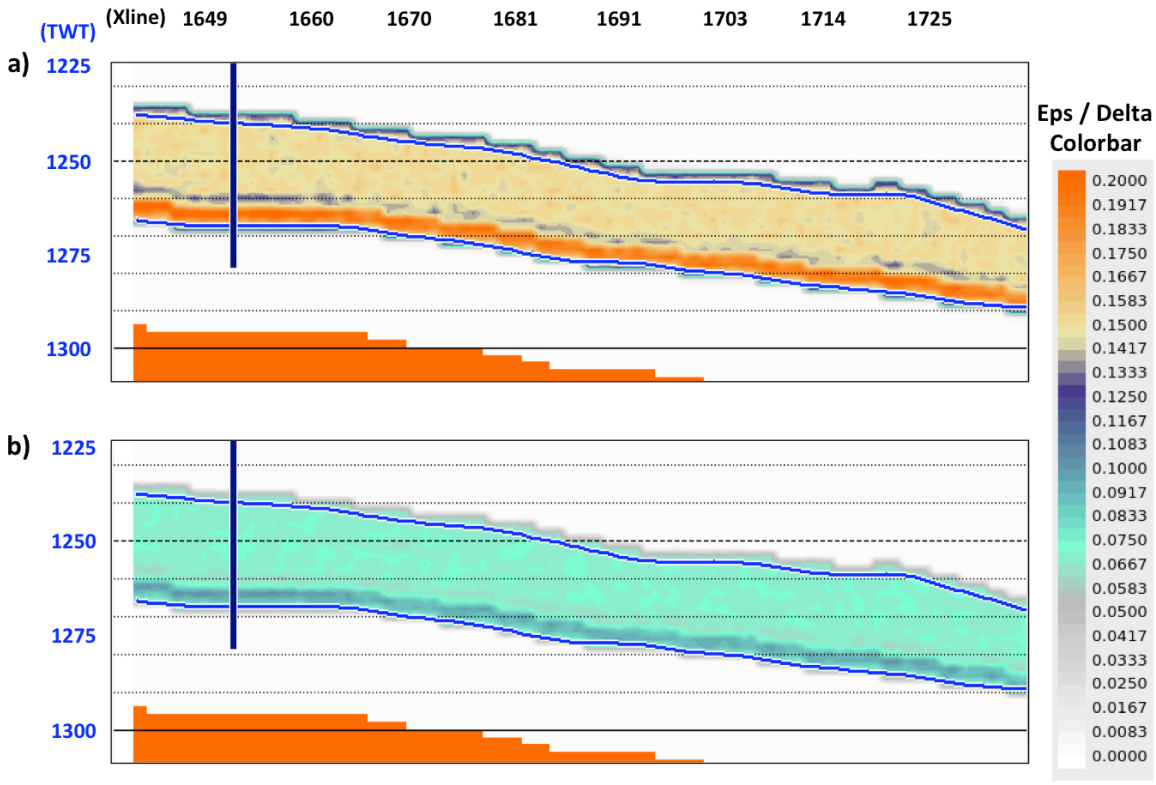

Figure 4.8. The GAIS inverted epsilon (a) and delta (b) at IL690 in two way travel time. The inserted blue line is well path of B4. In both figures the horizontal blue lines from top to bottom, represent horizon Austin Chalk, Eagle Ford, and Buda. The inversion window is from upper Austin Chalk to upper Buda. Both Austin Chalk and Buda are isotropic and Eagle Ford is vertical transverse isotropic.

4.6 DISCUSSION AND CONCLUSIONS

Thin-bed effect and anisotropy are two influential factors in seismic characterization of Eagle Ford shale. Here I used the geostatistics guided GAIS inversion to resolve the thin bed problem. The high-resolution geostatistical initial model was built by sequential Gaussian simulation. The geostatistical models simulate small-scale vertical variations that are beyond seismic resolution. Using those as initial models compensates forthe band-limited nature of seismic data. GAIS is a combination of very fast annealing method and greedy importance sampling. It seeks the importance regions using GIS based on multiple parallel VFSA results, which are already close to the importance region; then it explicitly explores the target distribution by grid searching the importance region with fixed step length along axis parallel directions. . As to anisotropy, I used Ruger's VTI model to account for the anisotropy in forward modeling.

I applied this geostatistics guided inversion on pre-stack 3D seismic data to estimate the reservoir elastic properties and anisotropy parameters. The GAIS inversion results are compared with deterministic inversion done using a commercial software. The GAIS inversion clearly resolves the thin Lower Eagle Ford in P- and S- impedance. The sharp boundary and large impedance contrast between Eagle Ford and Buda are very clear in GAIS inverted impedances. Also, the low impedance thin- bed inside Austin Chalk is also resolved by GAIS inversion. However, these features are not shown in deterministic inversion result. In addition, because of accounted anisotropy, the inverted S-impedance is significantly improved by GAIS. The GAIS inverted P- and S-impedances vary laterally, but the lateral continuities are preserved. The update of anisotropy from inversion is negligible. This is expected since I used the lab measured ϵ and δ as initial model.

The thin-bed issue and anisotropy are common issues in seismic reservoir characterization. The methods I applied on Eagle Ford shale could also applied to other reservoirs. Although I only showed the expectation value of model as the final result in this paper, the samples created in GAIS Step 3 samples form the target distribution, and the weights assigned in Step 4 represent the relative probability of corresponding samples. The histogram of these samples represents the target distribution, based on which quantitative uncertainty can be analyzed.

The algorithm used in this work can be considered as an alternative to a standard geostatistical simulation. Geostastical simulations simply estimate a field from using spatial statistics. Here I validate and modify the geostastistically simulated models by matching seismic data. Unlike the conventional geostatistical inversion methods, our method is computationally fast, includes anisotropy and is able to estimate uncertainty rigorously.

Chapter 5: Conclusion and Future Work

5.1 CONCLUSIONS

A typical quantitative reservoir characterization process includes building up the relations between rock properties and elastic properties through rock physics modeling, inverting for elastic properties from seismic data, and inverting for rock properties by integrating seismic data and rock physics models. There are many quantitative reservoir characterization techniques for conventional reservoirs. However, challenges exist when extending these methods to unconventional reservoirs because of the complexity of shale. This dissertation investigates anisotropic rock physics modeling with shale's complex micro-scale fabric accounted for, and the geostatistics guided anisotropic seismic inversion to resolve thin beds of shale.

In Chapter 3, I presented a comprehensive three-step rock-physics approach to model the anisotropic elastic properties, accounting for the micro-scale fabric of the rock in terms of the complex composition, shape and alignment of clay minerals, pore space, and kerogen. This method also accounted for different pressure-dependent behaviors of P-waves and S-waves. The modeling provided anisotropic stiffnesses and pseudo logs of anisotropy parameters. The application of this method on the Upper Eagle Ford Shale showed that the clay content, kerogen content and porosity decrease the rock stiffness. The anisotropy increased with kerogen content, but the influence of clay content was more complex. Comparing the anisotropy parameter pseudo logs with clay content showed that clay content increases the anisotropy at small concentrations; however, the anisotropy stays constant, or even slightly decreases, as clay content continues to

increase. This result suggests that the preferred orientation of clay clusters is preserved at low clay concentration but vanishes at high clay concentration.

Chapter 4 presents a geostatistics guided seismic inversion method and its application on the Eagle Ford Shale. Thin beds and anisotropy are two important factors limiting the use of conventional seismic characterization for unconventional reservoirs. To address these issues, I used the geostatistics guided greedy annealing importance sampling (GAIS) inversion. The geostatistical models, based on well log data, simulate small-scale vertical variations that are beyond seismic resolution. This additional information compensates for the band-limited nature of seismic data. I used the geostatical models as a priori models and then applied the GAIS inversion to quickly search for the most probable pseudo-logs at all surface locations. GAIS used the greedy importance sampling method based on multiple parallel very fast simulated annealing (VFSA) results; then it explicitly explored the target distribution by grid searching of the important regions with a fixed step length along the axis parallel directions. This method performed an optimal balance between computational efficiency and accuracy of estimation. To account for anisotropy, Ruger's VTI model was applied in forward modeling. This geostatistics guided inversion was applied on a pre-stack 3D seismic data to estimate the reservoir elastic properties and anisotropy parameters of the Eagle Ford shale. Compared to the conventional deterministic method inverted impedances, the geostatistics guided GAIS inversion clearly resolved the lower Eagle Ford in the inverted impedance volume. The sharp boundary and large impedance contrast between the Eagle Ford and Buda are also very clear in GAIS inverted impedances. Compared to it, the inverted impedances derived by the deterministic method appear as several thick blocks, whose layer boundaries were ambiguous. In addition, because anisotropy was accounted for, the quality of the inverted S-impedance is significantly improved.

This dissertation involved modeling and inversion at various scales. The developed rock physics model was at the grain scale. However, the composition used in the rock physics modeling was at the log scale, and the pressure dependent P- and S-wave behaviors were measured at the core scale. The rock physics modeled stiffnesses were at the log scale. The geostatistical models used as prior models for GAIS inversion were at the log scale, while the surface seismic data was at the seismic scale. Therefore, the inverted impedances were at a scale between the well log and the seismic scale. The integration of multi-scale data and modeling increases the uncertainty of modeled stiffnesses and inverted stiffnesses.

The main contributions of this dissertation include multiple aspects. Firstly, in the rock physics modeling, I developed a comprehensive method to model the anisotropic elastic properties. This new method accounts for the micro-scale fabric of the rock in terms of the complex composition, shape and alignment of clay minerals, pore space, and kerogen; also, the different pressure-dependent behaviors of P-waves and S-waves are accounted for. Most of the previous studies only accounted for part of the micro-scale fabric. In addition, most of those previous studies using effective rock physics modeling methods did not account for the pressure effect. Secondly, in this dissertation, the anisotropic geostatistics model is introduced to seismic inversion for resolving thin beds. Most of the previous studies focused on improving the seismic resolution itself to resolve the thin beds. However, because of the band limited nature of seismic data and the noise in data, these methods did not work well in many cases. By integrating the small-scale vertical variation from well logs with seismic data, the thin beds could be clearly identified in the inverted impedance volumes. Finally, anisotropy was modeled and accounted for in both rock physics modeling and seismic inversion. The rock physics modeling showed that anisotropy was highly correlated with clay content and kerogen;

the anisotropy information could help to identify high clay areas or zones with high kerogen content. Beside that, anisotropy has a first order influence on S-wave and converted P-S wave. Therefore, including anisotropy in seismic inversion significantly improves the inverted S-wave impedance accuracy. The improvement was observed on the Eagle Ford Shale seismic inversion as shown in Chapter 4.

5.2 FUTURE WORK

A standard quantitative reservoir characterization process includes building up the relations between rock properties and elastic properties through rock physics modeling, inverting for elastic properties from seismic data, and inverting for rock properties from both seismic data and rock physics models. This dissertation discussed the implementation of first two steps in unconventional reservoir characterization, but the last step has not been investigated yet. The grid search method could provide a good approach for the last step. The rock physics modeling provided the relationship between anisotropic elastic properties and rock properties (e.g. porosity, clay content) at the log scale, and the seismic inversion provided 3D anisotropic elastic property volumes at the seismic scale. The grid search method could estimate the seismic scale rock properties and the associated uncertainties based on the seismic inverted elastic properties and the rock physics models. In the grid searching process, P- and S-impedances from the rock-physics models could be compared with the ones inverted from the seismic data. The modeled impedances that satisfied specific criteria could provide the estimated rock properties. For each trace at each time, grid searching would provide a large number of estimated rock properties based on the objective function. The mean value and standard deviation were calculated for each rock property at each point. The standard deviation

would show the uncertainty of the estimations spatially and vertically. Using the grid search method to invert for rock properties from both seismic data and rock physics models could be a good future research direction.

Appendix A: Influence of Anisotropy on Surface Seismic Data

Anisotropy influences seismic waves by affecting their amplitude, travel time and ray paths; further, it introduces and propagates errors in inversion and amplitude versus offset (AVO) analysis that assume isotropy (Sayers, 2005). In addition, works by Crampin (1981, 1985), Lynn and Thomsen (1986), and others demonstrated that anisotropy has a first-order influence on shear and mode-converted PS-waves. Table A.1 shows the laboratory-measured anisotropy for Eagle Ford Shale in our study area. In this appendix, I firstly show the influence of anisotropy on seismic waveforms by comparing the synthetic seismograms on a four layer earth model using both vertical transverse isotropic (VTI) and isotropic models. Secondly, I compare the calculated P-P reflection coefficient at the Lower Eagle Ford – Buda interface computed by using an exact analytical formula and Ruger's (1997) approximation.

Anisotropy	Upper Eagle Ford	Lower Eagle Ford
ε	0.15±0.05	0.31±0.08
γ	0.13±0.05	0.32±0.09
δ	0.07±0.03	0.15±0.04

Table A.1: laboratory-measured anisotropy for Eagle Ford Shale in our study area.

Graebner (1992) derived the analytical solution of plane-wave reflection and transmission coefficients, as functions of ray parameters, for a transversely isotropic

system. These solutions worked well on systems where the ray parameter is the independent variable. In the paper, he presented the solutions for both a welded contact and a fluid-solid contact. I applied his welded contact solution to simulate synthetic seismograms, and compared those with the synthetic seismograms simulated using an isotropic model (Figure A.1). From Graebner (1992), the reflection coefficient of the downward propagating wave can be calculated as

$$R = P_1^{-1}[Q_1P_1^{-1} + Q_2P_2^{-1}]^{-1}(Q_1P_1^{-1} - Q_2P_2^{-1})P_1, \quad \text{(A1)}$$

where subscript 1 and 2 represent properties of upper layer and lower layer respectively, and *R, P, Q* are all matrices such as

$$R = \begin{pmatrix} r_{pp} & r_{sp} \\ r_{ps} & r_{ss} \end{pmatrix}, \quad \text{(A2)}$$

where subscript *pp*, *sp*, *ps*, and *ss* represent P-P wave, S-P mode converted wave, P-S mode converted wave, and S-S wave respectively, r represents reflectivity coefficient.

$$P = \begin{pmatrix} l_\alpha & m_\beta \\ c & d \end{pmatrix}, \quad Q = \begin{pmatrix} m_\alpha & -l_\beta \\ a & b \end{pmatrix}. \quad \text{(A3)}$$

where *l, m, a, b, c, d* are functions of density, velocity and anisotropy for the corresponding layer, subscript α and β represent P- and S-wave respectively.

The earth model (Figure A.1a) used in this simulation contains four layers, which are the Austin Chalk, Upper Eagle Ford, Lower Eagle Ford, and Buda. Among these layers, the Austin Chalk, and Buda are set to be isotropic; the Upper Eagle Ford and Lower Eagle Ford are VTI media, whose Thomsen parameters are set at the average values of the laboratory-measured anisotropy shown in Table A.1. Thickness, density, and velocities of these four layers are shown in Table A.2.

	Thickness (m)	Density (g/cm^3)	Vp (km/s)	Vs (km/s)
Austin Chalk	206.9	2.65	4.91	2.61
Upper Eagle Ford	57.9	2.5	4.42	2.5
Lower Eagle Ford	13.4	2.3	4.02	2.3
Buda	27.2	3	5.68	3

Table A.2: Thickness, density, and velocities of the four layers in earth model (Figure A.1a).

Figure A.1 shows the comparison between the synthetic seismograms generated based on VTI earth model (Figure A.1b) and on isotropic earth model (Figure A.1b). The seismograms based on the VTI earth model uses Graebner's (1992) analytical reflection coefficient solutions for welded contact layers. There are three reflections shown in Figures A.1b and A.1c, which are the top of Upper Eagle Ford, the top of Lower Eagle Ford, and the top of Buda. The P-P reflection shows a stronger AVO effect on VTI earth model than isotropic earth model. In addition, the P-S reflection behaviors are very different between using the VTI earth model and isotropic earth model. In seismograms generated from the VTI earth model (Figure A.1b), the P-S reflection is weak at near offset, and becomes stronger towards mid-offset. The strongest reflection shows at an offset of nearly 1.62km. The P-S reflection on isotropic earth model (Figure A.1c) is

much weaker than it on isotropic earth model (Figure A.1b). This study suggests that anisotropy is an important influential factor on seismic data for the Eagle Ford Formation, and it should be accounted for in seismic inversion.

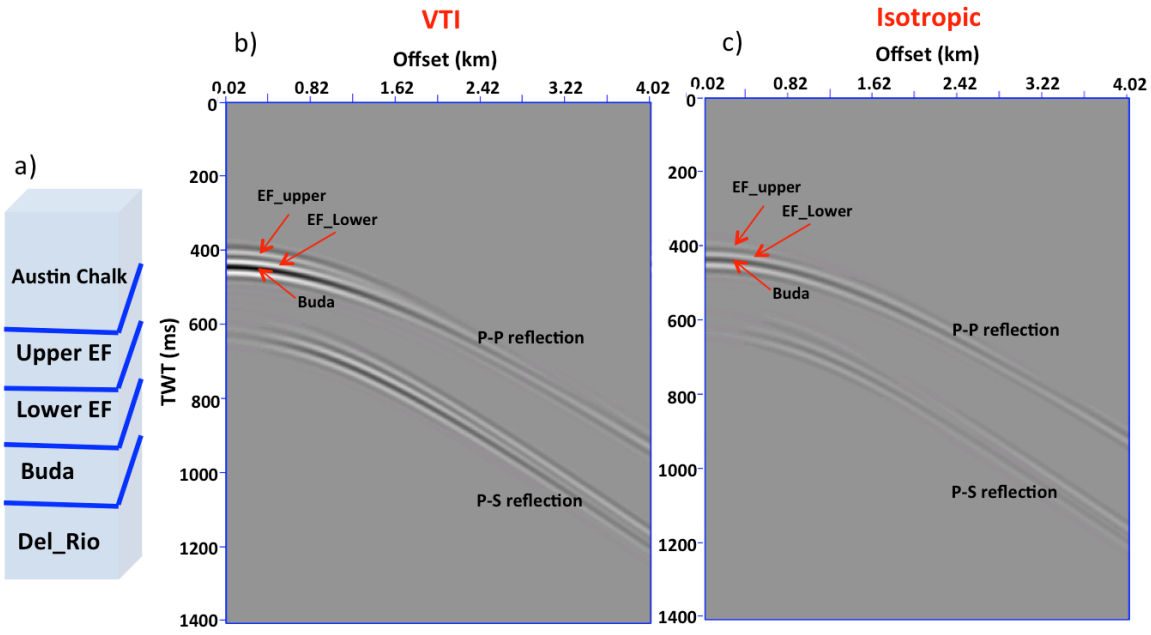

Figure A.1: a) Earth model. The earth model used in this simulation contained four layers. Both Upper and Lower Eagle Ford were set as VTI formation; Austin Chalk, and Buda were set as isotropic formation; b) Synthetic seismograms of the earth model in a); c) control group. Synthetic seismograms using the earth model in a), but setting both Upper and Lower Eagle Ford as isotropic formation. The amplitude scale in c) is same as in b).

Although Graebner (1992) derived the analytical reflection coefficient solutions for VTI media, the solutions are very complex. Also, the solutions are computational expensive, since they contain several matrix inversion operations. Therefore, most reflection coefficients are calculated using different levels of approximation. I compared the calculated P-P wave reflection coefficients using Graebner's (1992) analytical solution with using Ruger's (1997) VIT approximation on the Lower Eagle Ford – Buda interface. The Buda formation was set as an isotropic formation, and the Lower Eagle Ford was set as a VTI formation whose Thomsen parameters were the average values of the laboratory-measured anisotropy shown in Table A.1. Figure A.2 shows the calculated P-P wave reflection coefficients using Graebner's solution, Ruger's approximation, and isotropic exact solution as a function of wave propagation angle. For angles less than 12 degrees, the calculated reflection coefficients using these three methods are same. The VTI solutions and isotropic solution start to diverge beyond 12 degree, and show clear differences after 20 degree. The calculated reflection coefficients using Graebner's solution and Ruger's approximation are similar from 0 to 35 degrees, and then they start to diverge. Since I used the seismic angle gathers with offset range 4 to 34 degrees for seismic inversion, there won't not be clear difference on inversion results between using Graebner's exact solution and Ruger's approximation.

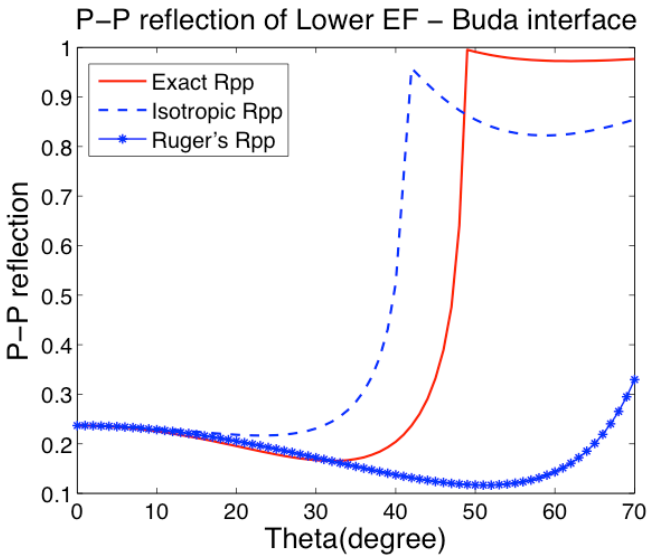

Figure A.2: Comparison of calculation P-P reflection coefficient on the Lower Eagle Ford – Buda interface using Graebner's analytical solution and Ruger's approximation. P-P reflection coefficient is plotted as a function of propagation angle. Red solid curve represents the calculated reflection coefficient using Graebner's solution, blue star curve represents the calculated reflection coefficient using Ruger's approximation, and blue dash curve represent the calculated reflection coefficient using isotropic exact solution.

References

Allan, A., W. Kanitpanyacharoen, and T. Vanorio, 2014, A multiscale methodology for the analysis of velocity anisotropy in organic-rich shale: Geophysics, **80**, 473-88.

Aplin A., I. Matenaar, D. Matenaar, and B.A.Van Der Pluijm, 2006, Influence of mechanical compaction and clay mineral diagenesis on the microfabric and porescale properties of deep-water Gulf of Mexico mudstones: Clays and Clay Minerals, **54**, 500–514.

Avseth, P., J. Dvorkin, G. Mavko, and J. Rykkje, 2000, Rock-physics diagnostic of North Sea sands: Link between microstructure and seismic properties: Geophysical Research Letters, **27**, 2761-2764.

Bachrach, R., C. Sayers, S. Dasgupta, et al., 2013, Recent Advances in the Characterization of Unconventional Reservoirs with Wide-Azimuth Seismic Data: Unconventional Resources Technology Conference, Denver, Colorado, USA, August 12-14, 2013.

Baker, D., K. Chawla, and R. Krizek, 1993, Compaction fabrics of pelites: experimental consolidation of kaolinite and implications for analysis of strain in slate: Journal of Structural Geology, **15**,1123–1137.

Bandyopadhyay, K., 2009, Seismic anisotropy: Geological causes and its implications to reservoir geophysics: Ph.D. Dissertation, Stanford.

Banik, N. C., 1984, Velocity anisotropy in shales and depth estimation in the North Sea basin: Geophysics, **49**, 1411–1419.

Banik, N. C., 1987, An effective parameter in transversely isotropic media: Geophysics, **52**, 1654–1664.

Berryman, J., 1992, Single-scattering approximations for coefficients in Biot's equations of poroelasticity: Journal of the Acoustical Society of America, **91**, 551–571.

Berryman, J., 1995, Mixture theories for rock properties, *in* T. J. Ahrens, Rock Physics and Phase Relations: A Handbook of Physical Constants: American Geophysical Union Reference Self 3, 205-228.

Bosch, M., T. Mukerji, and E. Gonzalez, 2010, Seismic inversion for reservoir properties combining statistical rock physics and geostatistics: A review: Geophysics, **75**, 165 – 176.

Chalmers, G., R. Bustin, and I. Power, 2012, Characterization of gas shale pore systems by porosimetry, pycnometry, surface area, and field emission scanning electron microscopy/transmission electron microscopy image analyses: Examples from the Barnett, Woodford, Haynesville, Marcellus, and Doig units: AAPG Bullet, **6**, 1099-1119.

Chapman, M., 2003, Frequency-dependent anisotropy due to meso-scale fractures in the

presence of equant porosity: Geophysical Prospecting, **51**, 369–379.

Chen, S. S., D. L. Donoho, and M. A. Saunders, 2001, Atomic decomposition by basis pursuit: Society for Industrial and Applied Mathematics Review, **43**, 1,129–159.

Cooke, D. and Schneider, W., 1983, Generalized linear inversion of reflection seismic data: Geophysics, **48**, 6, 665-676.

Crampin, S., 1981, Areview of wave motion in anisotropic and cracked elastic media: Wave Motion, **3**, 343–391.

Crampin, S., 1985, Evaluation of anisotropy by shear-wave splitting: Geophysics, **50**, 142–152.

Deutsch, C. V., and A. G. Journel, 1998, GSLIBL geostatistical software library and user's guide, 2nd edn: Oxford University Press, New York.

Dewhurst, D. N., and A. F. Siggins, 2006, Impact of fabric microcracks and stress field on shale anisotropy: Geophysical Journal International, **165**, 135–148.

Goldberger, A., 1962, Best linear unbiased prediction in the generalized linear regression model: Journal of the American Statistical Association, **57**, 298, 369 - 375.

Goovaerts, P., 1997, Goestatistics for natural resources evaluation: Oxford University Press, New York.

Graebner, M., 1992, Plane-wave reflection and transmission coefficients for a transversely isotropic solid: Geophysics, **57**, 1512 – 1519.

Grana, D., and E. D. Rossa, 2010, Probabilistic petrophysical-properties estimation integrating statistical rock physics with seismic inversion: Geophysics, **75**, O21-O37.

Haas, A., and O. Dubrule, 1994, Geostatistical inversion - A sequential method of stochastic reservoir modeling constrained by seismic data: First Break, **12**, 561–569.

Heidari, Z., and C. Torres-Verdin, 2013, Inversion-based method for estimating total organic carbon and porosityand for diagnosing mineral constituents from multiple well logs in shale-gas formations: Interpretation, **1**, 113-123.

Hentz, T., S. Ruppel, 2010, Regional Lithostratigraphy of the Eagle Ford Shale: Maverick Basin to East Texas Basin: Gulf Coast Association of Geological Societies Transactions, **60**, 325-337.

Ho, N.C., D.R. Peacor, and B.A. Van Der Pluijm, 1995, Reorientation of phyllosilicates in the mudstone-to-slate transition at Lehigh Gap, Pennsylvania: Journal of Structural Geology, **17**, 345-356.

Ho, N.C., D.R. Peacor, and B.A. Van Der Pluijm, 1996, Contrasting roles of detrital and authigenic phyllosilicates during slaty cleavage development: Journal of Structural Geology, **18**, 615-623.

Ho N.C., D.R. Peacor, and B.A. Van Der Pluijm, 1999, Preferred orientation of phyllosilicates in Gulf Coast mudstones and relation to the smectite-illite transition: Clays and ClayMinerals, **47**, 495–504.

Hentz, T., S. Ruppel, 2010, Regional Lithostratigraphy of the Eagle Ford Shale: Maverick Basin to East Texas Basin: Gulf Coast Association of Geological Societies Transactions, **60**, 325-337.

Hornby, B. E., 1998, Experimental laboratory determination of the dynamic elastic properties of wet, drained shales: Journal of Geophysical Research: Solid Earth, **103**, 29945–29964.

Ingber, L. 1989, Very fast simulated re-annealing: Mathematical and Computer Modelling, **12**, 8, 967-973.

Jones, L., and H. Wang, 1981, Ultrasonic velocities in Cretaceous shales from the Williston basin: Geophysics, **46**, 288-297.

Jiang, M., and K. T. Spikes, 2013a, Estimation of reservoir properties of the Haynesville Shale by using rock physics modeling and grid searching: Geophysical Journal International, **195**, 315-329.

Jiang, M., and K. T. Spikes, 2013, Characterizing the reservoir properties of the Haynesville Shale using rock-physics modeling and grid searching: Geophysical Journal International, **195**, 315-239.

Jiang, M., Seismic reservoir characterization of the Haynesville Shale: rock-physics modeling, prestack seismic inversion and grid search: Ph.D. Dissertation, The University of Texas at Austin.

Johansen, T., B. Ruud, and M. Jakobsen, 2004, Effect of grain scale alignment on seismic anisotropy and reflectivity of shales: Geophysical Prospecting, **52**, 133-149.

Jones, L., and H. Wang, 1981, Ultrasonic velocities in Cretaceous shales from the Williston basin: Geophysics, **46**, 288-297.

Johnston, J., N. Christensen, 1995, Seismic anisotropy of shale: Journal of geophysical research, **100**, 5991-6003.

Kanitpanyacharoen, W., H.R. Wenk, F. B. Kets, C. Lehr, and R. Wirth, 2014, Linking preferred orientations to elastic anisotropy in Muderong Shale, Australia: Geophysics, **80**, 9–19.

Kanitpanyacharoen, W., R. Vasin, H. R. Wenk, C. Lehr, and N. Dewhurst, 2011, Texture and anisotropy of Qusaiba Shales, Saudi Arabia: Geophysical Prospecting, **59**, 536–556.

Krige, D. G., 1951, A statistical approach to some mine valuations and allied problems at the Witwatersrand: M.S. thesis, University of Witwatersrand, South Africa.

Lynn, H. B., and L. Thomsen, 1986, Shear wave exploration along the principal axis: 56th Annual International Meeting, SEG, Expanded Abstracts, 474–476.

Matheron, G., 1970, La theorie des variables regionalisees, et ses applications. Les cahiers du Centre de Morphologie Mathematique de Fontanebleau, Fascicule 5.

Marfurt, K. J., and R. L. Kirlin, 2001, Narrow-band spectral analysis and thin-bed tuning: Geophysics, **66**, 1274–1283.

Matthies, S., H. G. Priesmeyer, and M. R. Daymond, 2001, On the diffractive determination of single-crystal elastic constants using polycrystalline samples: Journal of Applied Crystallography, **34**, 585–601.

Mavko, G., T. Mukerji, J., Dvorkin, 2009, The Rock-physics Handbook: Tools for Seismic Analysis of Porous Media: Cambridge University Press.

Morris, P., 1969, Averaging fourth rank tensors with weight functions: Journal of Applied Physics, **40**, 447-449.

Mukerji, T., A. Jorstad, P. Avseth, et. al, Mapping lithofacies and pore-fluid probabilities in a North Sea reservoir: Seismic inversions and statistical rock physics: Geophysics, **66**, 988-1001.

Norris, A.N., 1985, A differential scheme for the effective moduli of composites: Mechanics of Materials, **4**, 1-16.

O'Connell, R. J. and B. Budiansky, 1974, Seismic velocities in dry and saturated cracked solids: Journal of Geophysical Research, **82**, 5719–5735.

Owens, W., 1973, Strain modification of angular density distributions: Tectonophysics, **16**, 249–261.

Partyka, G. A., 2005, Spectral decomposition: SEG Distinguished Lecture.

Portniaguine, O., and J. P. Castagna, 2004, Inverse spectral decomposition: 74th Annual International Meeting, SEG, Expanded Abstracts, 1786–1789.

Puryear, C. I., and J. P. Castagna, 2006, An algorithm for calculation of bed thickness and reflection coefficients from amplitude spectrum: 76thAnnual International Meeting, SEG, ExpandedAbstracts, 1767–1770.

Ren, Q., and K. Spikes, 2014, Anisotropic rock-physics modeling for the Haynesville Shale: 82nd Annual International Meetings, SEG, Expanded Abstracts, 2947-2951.

Riel, P. V., and A. J. Berkhout, 1985, Resolution in seismic trace inversion by parameter estimation: Geophysics, **50**, 1440–1455.

Roe, R., 1965, Description of crystallite orientation in polycrystalline material. III. General solution to pole figure inversion: Journal of Applied Physics, **36**, 2024–2031.

Ruger, A., 1997, P-wave reflection coefficients for transversely isotropic models with vertical and horizontal axis of symmetry: Geophysics, **62**, 3, 713 – 722.

Sayers, C., 1994, The elastic anisotropy of shales: Journal of Geophysical Research, **99**, 767-774.

Sayers, C., 2005, Seismic anisotropy of shales: Geophysical Prospecting, **53**, 667-676.

Sayers, C. M., and L. D. den Boer, 2011, Rock physics-based relations for density and S-velocity versus P-velocity in deepwater subsalt Gulf of Mexico shales: The Leading Edge, **30**, 1376–1381.

Schuurmans, D. and F. Southey, 2000, Monte Carlo inference via greedy importance sampling: UAI'00 Proceedings of the Sixteenth conference on Uncertainty in artificial intelligence, 523 – 532.

Sen, M. K and P. L. Stoffa, 1995, Global Optimization Methods in Geophyscial Inversion: Elservier Science Publications.

Sondergeld, C., R. Ambrose, C. Rai, and J. Moncrieff, 2010, Micro-structural studies of gas shales: SPE Unconventional Gas Conference, SPE, Conference Paper, SPE 131771.

Sone, H., 2012, Mechanical properties of shale gas reservoir rocks and its relation to the in-situ stress variation observed in shale gas reservoir: Ph.D. Dissertation, Stanford.

Sone, H., and M.Zoback, 2013, Mechanical properties of shale-gas reservoir rocks — Part 1: Static and dynamic elastic properties and anisotropy: Geophysics, **78**, P. D381-D392.

Spikes, K., T. Mukerji, J. Dvorkin, and G. Mavko, 2007, Probabilistic seismic inversion based on rock-physics models.

Srivastava, R. and M. K. Sen, 2010, Stochastic inversion of pre-stack seismic data using fractal based initial models: Geophysics, **75**, 3, R47-R59.

Thomsen, L., 1986, Weak elastic anisotropy: Geophysics, **51**, 1954–1966.

Vasin, R., H. R. Wenk, W. Kanitpanyacharoen, S. Matthies, and R. Wirth, 2013, Elastic anisotropy modeling of Kimmeridge shale: Journal of Geophysical Research: Solid Earth, **118**, 3931–3956.

Vernik, L., and A. Nur, 1992, Ultrasonic velocity and anisotropy of hydro- carbon source rocks: Geophysics, **57**, 727–735.

Vernik, L., and X. Liu, 1997, Velocity anisotropy in shales: A petrophysical study: Geophysics, **62**, 521-532.

Vernik, L., and J. Milovac, 2011, Rock physics of organic shales: The Leading Edge, **30**, 318-323.

Wang, Z., 2002, Seismic anisotropy in sedimentary rocks, part 2: Laboratory data*:* Geophysics, **67**, 1423-1440.

Wenk H. R., M. Voltolini, H. Kern, T. Popp and M. Mazurek, 2008, Anisotropy in shale from Mont Terri: The Leading Edge, **27**, 742–748.

Widess, M. B., 1973, How thin is a thin bed?: Geophysics, **38**, 1176-1180.

Xu, W., T. Tran, R. Srivastava, and A. Journel, 1992, Integrating seismic data in reservoir modeling: the collocated cokriging alternative: SPE Unconventional Gas Conference, SPE, Conference Paper, SPE 24742.

Xue, Y., M. K. Sen and Z. Deng, 2011, A new stochastic inference method for inversion of pre-stack seismic data: 79nd Annual International Meetings, SEG, Expanded Abstracts, 2757 - 2761.

Xue, Y., 2013, Novel stochastic inversion methods and workflow for reservoir characterization and monitoring: Ph.D. Dissertation, The University of Texas at Austin.

Zhang, R., and J. Castagna, Seismic sparse-layer reflectivity inversion using basis pursuit decomposition: Geophysics, **76**, 147 - 158.

Vita

Qi Ren received her B.S. degree in Applied Physics from the University of Science and Technology of China in Hefei, Anhui, China in 2010. In August 2010, she entered the University of Texas at Austin as a Ph.D. student for physics, and transferred to Jackson School of Geosciences as a Ph.D. student for geophysics in January 2012.

Email: qiren@utexas.edu

This dissertation was typed by Qi Ren.